Fabrication-aware structural optimisation of lattice additive-manufactured with robot-arm

Kam-Ming Mark Tam*, Daniel J. Marshall and Mitchell Gu

Department of Architecture,
Massachusetts Institute of Technology,
77 Massachusetts Avenue,
Cambridge, MA 02139, USA
Email: kmmt@mit.edu
Email: djmm@mit.edu
Email: mitchgu@mit.edu
*Corresponding author

Jasmine Kim

Segal Design Institute, McCormick School of Engineering,
Northwestern University,
2133 Sheridan Road, Room 1.325,
Evanston, IL 60208, USA
Email: jasminekim2018@u.northwestern.edu

Yijiang Huang, Justin Lavallee and Caitlin T. Mueller

Department of Architecture,
Massachusetts Institute of Technology,
77 Massachusetts Avenue,
Cambridge, MA 02139, USA
Email: yijiangh@mit.edu
Email: jalavall@mit.edu
Email: caitlinm@mit.edu

Abstract: Architectural structures achieving high strength and stiffness with intelligent, but intricate geometry may now be materialisable through additive manufacturing (AM). However, conventional layer-based AM also produces parts with inconsistent structural strength – thereby limiting AM's end-use applications. Expanding on robotics-enabled AM techniques addressing this limitation, a novel design-fabrication framework for producing structurally optimised lattices is presented here. Lattices are geometrically morphed to maximise their structural stiffness-to-weight ratio while respecting fabrication constraints imposed by the robotic printing process, and converted into tool-paths for PLA extrusion with a custom-built end effector mounted on an industrial robot arm. The printing process leverages thermal imaging for

calibration, and develops a novel joint detail to increase the reliability and load-transfer capabilities of the print. Together, these techniques and methods – validated through comparative structural load testing – show promise for architecture-scale AM that combines structurally driven geometry with complexity-agnostic materialisation in new and exciting ways.

Keywords: cellular material; lattice; additive manufacturing; FDM; fused deposition modelling; robotics; octet lattice truss; conformal lattice; 3-D truss; 3-D printed joints; bonding strength; structural load testing.

Biographical notes: Kam-Ming Mark Tam is an Integration Engineer at Thornton Tomasetti's CORE Studio and a researcher at the Digital Structures research group (DS) of Massachusetts Institute of Technology's (MIT) Building Technology (BT) programme, where he investigates approaches for design space exploration that combine both structural and fabrication considerations. Specifically, he has developed methods to simplify the design modelling and analyses of complex structural systems, and robotic-enabled additive manufacturing (AM) techniques to create high-performance AM-produced parts. He earned a MEng in Civil Engineering from MIT, and a MArch and a HBAS (with Economics Minor) from the University of Waterloo. He has taught in the Singapore University of Technology and Design and Pratt Institute, and practiced in several architectural firms.

Daniel J. Marshall completed his BA (Hons.) in Architecture at the University of Cambridge – graduating with a starred first in 2014. He then spent the subsequent year working at Niall McLaughlin Architects in London, where he primarily worked on the conversion of the Grade I listed Radcliffe Infirmary Building for University of Oxford. Since Marshall began his MArch studies at MIT in 2015, he has centred his research on computational fabrication – working as a Research Assistant at Professor Caitlin Mueller's DS, and at Professor Brandon Clifford's Cyclopean Masonry.

Mitchell Gu is a undergraduate SB candidate studying mechanical engineering, electrical engineering, and computer science at MIT. He is an enthusiastic maker of electromechanical devices and programmer for electronics and robotics; he is passionate about their applications in the design exploration of architectural spaces. To that end, he has worked with DS to develop layer-free and structurally informed AM techniques–combining his background and skills in both the building of hobbyist 3-D printers and robotic toolpath planning.

Jasmine Kim grew up in both the USA and South Korea and graduated from Southern Methodist University with a BS in Physics and Mathematics. She is currently a degree candidate for MS in Engineering Design Innovation at Northwestern University. With academic experience in computer science, physics, and architecture. Her research seeks to combine science and technology to create human-centred designs for real-life problems.

Yijiang Huang is a researcher working at the intersection of mathematics, robotics and building construction. Currently a Research Assistant at DS, and a SM candidate in MIT's BT programme, his research broadly focuses on the application of optimisation in building construction, such as the development of algorithms to determine the construction sequencing and associated robotic motion and toolpath planning required in robotics-enabled construction processes. He earned a BS in Applied Mathematics from University of Science and Technology of China, where he led a SIGGRAPH project in the Graphics and Geometric Computing Laboratory.

Justin Lavallee is the Director of the Architecture Shops at the MIT School of Architecture and Planning. As a Technical Instructor, He teaches a fabrication course to first-year MArch students and is involved in fabrication related workshops and studio courses. He also plans the ongoing growth and development of the fabrication facilities within the Department of Architecture. He received a MArch from the Harvard Graduate School of Design in 2010.

Caitlin T. Mueller is a researcher, designer, and educator working at the interface of architecture and structural engineering. She is currently an Assistant Professor at the MIT's Department of Architecture and Department of Civil and Environmental Engineering – in the Building Technology programme, where she leads the Digital Structures (DS) research group. She earned a PhD in Building Technology from MIT, a SM in Computation for Design and Optimisation from MIT, an MS in Structural Engineering from Stanford University, and a BS in Architecture from MIT, and has practiced at several architecture and engineering firms across the USA.

1   Introduction

Additive manufacturing (AM) offers unprecedented means for achieving geometrical complexity at the architectural scale – enabling mass customisation and endless flexibility. For architectural designers and structural and mechanical engineers, the advances in AM technologies offer significant research opportunity to investigate the analysis, generation and fabrication of cellular material (CM). The key advantages offered by CM are high strength-to-weight ratio (Gibson and Ashby, 1999), in addition to good absorption, and thermal and acoustic insulation properties (Nguyen et al., 2012). Despite CM's well-known advantageous mechanical properties, its use at scale conducive to architecture has remained limited in conventional industrial and manufacturing processes. This owes to a lack of (1) structural design methods for considering fabrication constraints, (2) modelling methods appropriate for the optimisation of complex 3-D structures with large number of design variables, and (3) experimental testing methods for evaluating, calibrating and validating the implementation of CM design and production methods.

   The work presented here addresses these fundamental problems by contributing a novel framework for robotics-enabled CM that encompasses design, optimisation, fabrication, and load testing. The focus is on a subclass of CM known as lattice cellular material (LCM), which are structural systems built from repeating cells of struts and nodes. In contrast to existing research centred on the development of numerical methods or experimental analyses, the presented research articulates the entire design-fabrication

workflow – emphasising methods for designers to creatively explore the LCM design space. On the design front, computational techniques are formalised for modelling LCM geometries and variation. An optimisation strategy is developed to accommodate fabrication constraints and robotic programming strategies. For fabrication, custom-built fused deposition modelling (FDM) equipment additively manufactures the designed LCM, and experimental techniques help fine-tune the computational design and fabrication methods. Lastly, physical experimental validation is done using a series of comparative structural load tests – providing results that demonstrate the potential for 3D printing as a means of fabricating end-use, high-functioning structures.

2 Literature review

2.1 Cellular material and additive manufacturing limitations

Cellular materials are classified by the nature of the internal voids: they are either stochastic (Figure 1(1.a)), which include foam-based materials, or ordered (Figure 1(1.b)), which includes materials like honeycombs and lattice (Evans et al., 2001). Ordered CM, such as LCM, possess a number of properties desirable in design applications, such as geometric regularity and computational simplicity – qualities lending to their useful application in design and engineering. Additionally, they have superior strength properties over stochastic ones (Ashby, 2000) (Figure 1(3)), which are attributed primarily to their primary mechanisms of structural action: while stochastic CM typically behaves in bending, the structural action in LCM is predominantly axial (Desphande et al., 2001).

The past several decades had seen a resurgence of interest devoted to the research of designed LCM in multiple disciplines. Metallurgists Ashby and Gibson (1983) provided the field's authoritative compilation of documentation and analyses on the mechanical behaviour of a variety of cellular material. In architecture, Chilton (2000) documented full-scale LCM implementation strategies as space truss. All practitioners have confronted one critical challenge: the production of LCM, which are geometrically complex, can incur significant costs when traditional manufacturing processes are used – thereby rendering their development impractical or uneconomical (Johnston et al., 2006).

Rapid advances in AM technologies, which offer capabilities such as parts consolidation, efficient cost scaling, and parts customisation, have partially allayed the concern related to the fabrication of LCM. However, current printing techniques, such as FDM, are problematic for fabricating end-use cellular structures, because these methods are layer-based (see Figure 2(2)), and can result in anisotropic printed artefacts whereby the strength capacity can be several times weaker across printed layers than within a single layer (Figure 2(1)). Compounding the material limitation is a lack of methods for integrating and incorporating both fabrication planning and constraints in the design generation process (Brackett et al., 2011) – leading to a general disconnect in design between the behaviour of the printed parts at the scale of the geometry, topology and filament layout that consequently negates the benefits of structural optimisation (Tam and Mueller, 2017). These problems limit both the durability and end-use application of the 3-D printed cellular structures.

Figure 1   (1) Low-density cellular material type, which includes (1.a) stochastic; and (1.b)
ordered cellular material; (2) photograph of the lattice cellular material developed
in this research; and a (3) re-adapted Ashby plot of stiffness vs. material properties for
several key material groups
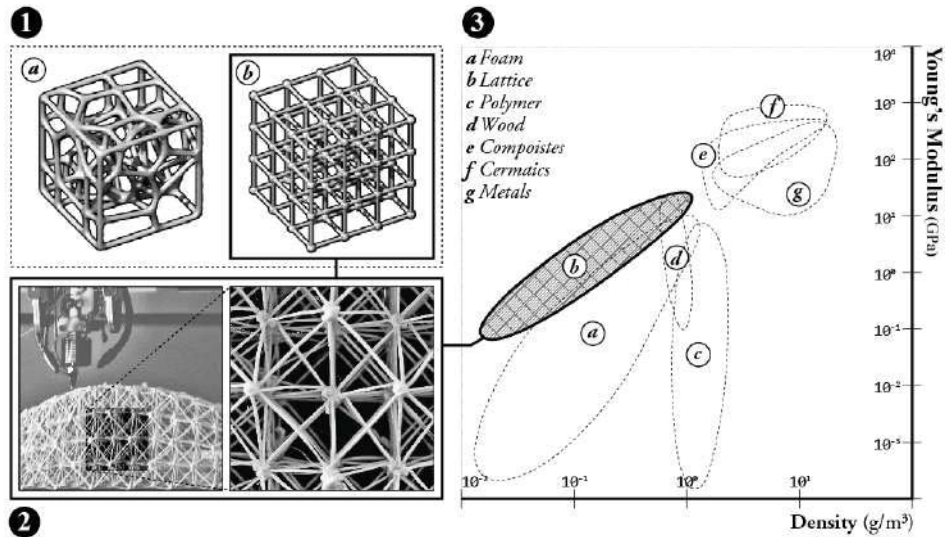
Source: Evans et al. (2001)

Figure 2   (Left) Photograph showing a LCM additive manufactured using a commercial layer-
based FDM platform: both fabrication and geometrical imperfections are evident; and
(Right) the failure generalisation of loads applied (1) parallel, or (2) traverse to filament
orientation
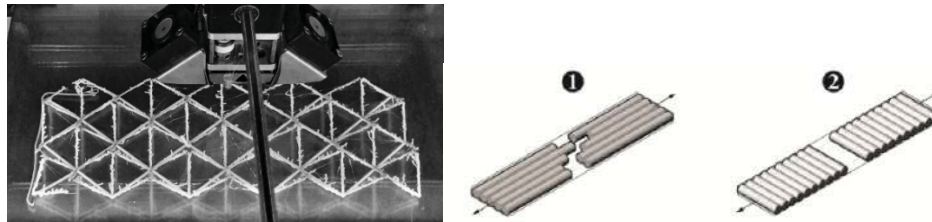
2.2   Research on additive manufactured lattice cellular material

A remedy to the problem of anisotropy has been pursued in recent research: instead of
printing in horizontal layers, the thermoplastic material can be deposited in true 3-D
space with industrial robotic arms along paths that can direct structural forces along
trajectories of material continuity – aligning force and filament orientation to eliminate
the need for structural action to traverse the weak bonds across discrete layers. Efforts in
these areas include dense lattice structures aligning to principle stress lines (Tam and
Mueller, 2017; Tam et al., 2016, 2017a; ICD, 2015), or conforming to complex geometric
volumes (Willmann et al., n.d.; Branch Technology, 2017; Festo, 2017). In the latter case,
the lattice may also serve as reinforcement or scaffolding respectively within or for a
composite material (Hack and Laurer, 2014).

Outside of design-oriented investigation, technical research on additive manufacturable LCM in mechanical engineering include experimental analyses of LCM parts additive manufactured using specific AM method (Beyer and Figueroa, 2016), analytical and numerical modelling methods (Deshpande et al., 2001; Johnston et al., 2006), and methods to generate lattice that conform to a given arbitrary design volume, such as the research of Chang (2010), and Nguyen et al. (2012), who respectively developed processes for element sizing optimisation and unit topology variation in conformal lattice, and Abd El Malek et al. (2005), who incorporated a *Heuristic Gradient Projection* technique to improve the optimisation of large 3-D space frames. In addition to the focus on stiffness maximisation, mechanical engineering researchers have developed methods for generating LCM to achieve compliant (Li et al., 2009; Zhou, 2010) and dynamic behaviour (Takezawa et al., 2005).

The additive manufacturing of lattice meso-structured parts constitutes another prominent research focus. Related works include Williams et al. (2005), who created a *Preliminary Selection Decision Support Problem Technique* to identify the manufacturing technologies most suitable for creating microstructures, and Rosen (2007), who articulated a comprehensive Design for Additive Manufacturing workflow to support part and specification modelling, process planning, and manufacturing simulations. Alternative and speculative fabrication processes were also developed: typically comprehensive in scope, such works include methods for producing periodic cellular metal sandwich structure (Evans et al., 2001), and research on cellular material that can be incrementally and reversibly assembled using digital material (Jenett, 2015; Jenett et al., 2016; Cheung and Gershenfeld, 2013).

In computer science, graphics researchers have similarly developed compliant-based methods to generate lattice meso-structured parts conforming to an arbitrary input volume by manipulating internal topology and material variation. Experimental testing are often extensively utilised in such research to provide validation on the proposed optimisation methods that predominately addresses non-linear structural behaviour. Examples include Schumacher et al. (2015), and Weeger et al. (2016), who developed methods to optimise the internal properties of lattice-based parts to achieve respectively variable elasticity across the material volume, or targeted large-scale deformation.

2.3 *Analysis of literature review*

Summarising the literature review in the preceding section, Figure 3 identifies the major topics of considerations in current research on additive manufactured LCM–indicating the relative popularity of various topics. The analysis reveals two key limitations in existing research on additive manufacturable LCM. Firstly, a general absence in consideration of the fabrication process is noticeable – particularly with regards to FDM, or robotics-enabled AM process. With most research generally focused on the development of novel computational methods, the framework for designing additive manufactured LCM is typically not articulated in full. Consequently, validation by experimental load testing remains rare, and few researches are able to offer improvement of the fabrication process, or material-specific fabrication techniques. Furthermore, the lack of incorporation of fabrication constraints in the design process contributes to limited considerations of the design's decomposition as fabrication instructions: there is limited research on the appropriate strategy for sequencing the production of LCM, and the effects of processing parameters on the mechanical strength of parts. Exceptions are

offered in the research of Jenett et al. (2016), and Evans et al. (2001); however, these examples develop alternative fabrication techniques that neither utilise the benefits, nor contribute to the development of standard AM.

Figure 3   Classification of research on additive manufactured LCM organised under the three major categories of (1) research methodology; (2) fabrication type; and (3) design aspects – with annotations indicating the relative popularity of the various subtopics and highlighting the focus of this research
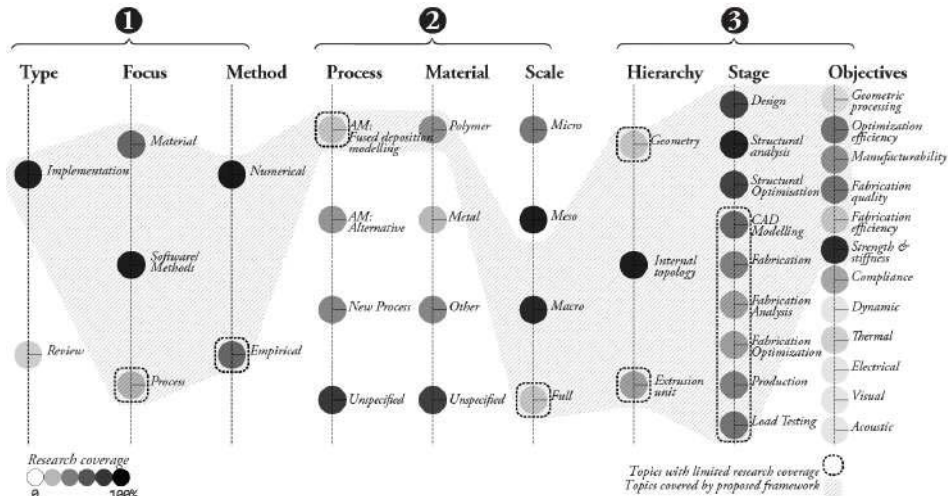
The second limitation relates to the design application of LCM design. Even though a large number of LCM-related computational methods have emerged, few researches are conceived explicitly with the objective to enable the open-ended design exploration of LCM design. As described later in Section 4.1.4, critical design aspects of LCM, such as global geometry and internal material composition, are often ignored, and there is a lack of methods appropriate for the characterisation of complex structures like LCM – systems with a large number of design variables. Finally, there is a lack of design implementation of LCM at architectural scale, or designs exploring complex geometry, as most implementations are based on simple surface-based design volume featuring large degree of planarity and constant thickness. Although promising progress has been made in architectural-oriented robotic research, many attempts are experimental proof-of-concepts predominantly concerned with the articulation of the innovative design-fabrication workflow, or the exploration of the aesthetic qualities incidental to the novel fabrication processes. Consequently, the production of full-scale LCM has generally lacked formalisation and remained performance-agnostic; their design and fabrication are seldom substantiated with structural logic.

3 Research methodology and lattice cellular material concepts

3.1 Objective and conceptual overview

As shown above, existing research in AM-based designed lattice structures has lacked an integration of design, structural and fabrication considerations. In response, the research presented here develops, consolidates and formalises a comprehensive workflow that encompasses the stages of design exploration, structural optimisation, robotic programming and fabrication, and structural load testing. The research is motivated to capitalise on the crucial relationship between geometry and structural behaviour to enable the structurally informed design space exploration of high-performance additive manufacturable LCM at architectural scales. Integrating fabrication development, techniques for materialising LCM are also developed, so that the fabrication method can be used reliably to create end-use functional parts at full-scale, such as building components, or mechanically meaningfully pieces for comparative load testing at the prototyping scale. Original contributions include a custom-developed extrusion module, novel tool-pathing strategies, a physical testing protocols to achieve calibration of fabrication and analytical parameters, and fabrication-aware optimisation strategies including a novel class of computational techniques – known as *global morphing techniques (GMT)* – to model geometrically complex LCM with large number of design variables.

Informing the structure of this paper is the generalised workflow of the robotics-enabled LCM design-fabrication process, which consists of: (1) Domain specification and computational LCM generation (Section 3.3.1), which uses an original interpolation algorithm (Section 3.3.1); (2) LCM Optimisation, which encompasses *GMT* devised to simplify design characterisation (Section 4.2.1), and strategies for considering fabrication constraints (Section 4.3); (3) Clustering and sequencing of LCM centre-line frame geometries (Section 5.4.1), and their conversion to fabrication instructions (Section 5.4.2), which refers to the custom extrusion module developed in the research (Section 5.3); (3) Robotics-enabled additive manufacturing of LCM parts (Section 7.2); and (4) Experimental load testing (Section 7.3). A primary contribution of the research is the iterative re-adaptation of (3) and (4) to generate feedback used to calibrate fabrication (Section 6.3.1) and analytical parameters (Section 6.4.2), and to develop improvements to the tool-pathing strategy to achieve LCM parts with greater mechanical strength and stiffness (Section 6.3.2) that are physically validated (Section 6.4.1).

3.2 Research scope and concepts review

3.2.1 Hierarchical design complexity

LCM are systems consisting of a set of beam elements or struts connected to a set of nodes. Figure 4 illustrates the multi-scale hierarchical design decomposition of LCM. The boundary geometry or volume defining the lattice material is shown in Figure 4(1). Composing the volume is a 3-D grid of unit-cells, which may be structured or unstructured, that act as the material's primary building block (see Figure 4(2)). Within each unit-cell (see Figure 4(3)), a truss structure consisting of nodes and beam elements are constructed according to the connectivity information of various unit-cell typology primitives (Figure 4(4)) – creating the final lattice structure (see Figure 4(5)).

Figure 4   Hierarchical decomposition of conformal lattice material – showing: (1) global
geometry; (2) subdivision of geometry into grid cells; (3) individual unit-cell; (4)
primitive topology module constructed within each unit-cell; and (5) final LCM with
module topology fully applied
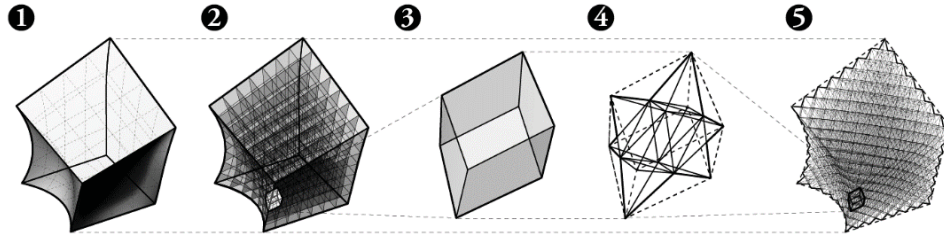
3.2.2   Conformal lattice generation

Two strategies are used to subdivide a design volume into unit-cells: LCM are either
uniform or conformal. In uniform lattice (see Figure 5(1)), the global geometry is
subdivided by a 3-D regular Cartesian grid of pre-defined density and orientation, thereby
creating both cuboid cells, and irregular polyhedron near the volumetric boundary. For
conformal lattices (see Figure 5(2)), the underlying 3-D grid structure is generated via
parameterisation – resulting in a tri-parameter grid of unit-cells in geometrical alignment
to LCM design volume. The proposed research develops conformal lattice, due to its
topological consistency and uniformity regardless of geometrical complexity.

Figure 5   Various LCM subdivision approaches applied on an irregular 3-D hexahedra-like
volume, which includes (1) uniform and (2) conformal decomposition
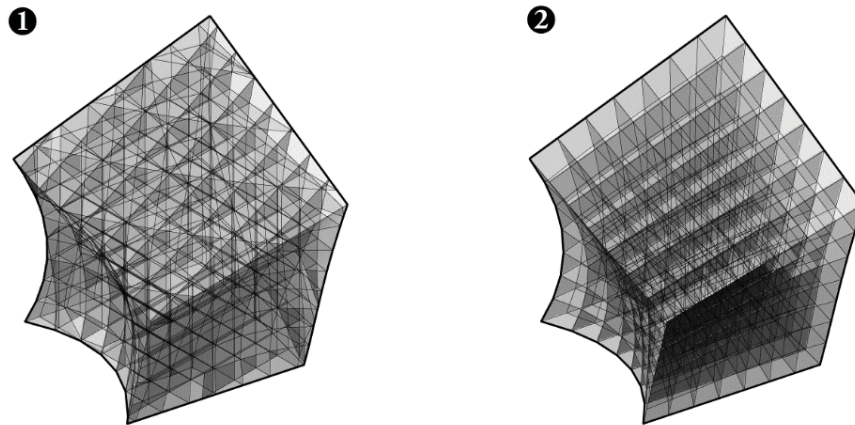
3.2.3   Geometric scope and characteristics

Using the presented framework, LCM can be generated to fill any closed hexahedra-like
geometry, or volume defined by 6 boundary surfaces (Figure 6(1)). The focus on
hexahedra-like geometries enables the direct adaptation of the standard tri-parameter data
organisation of 3-D Cartesian space – thereby facilitating the parameterised subdivision
of a design volume into a structured 3-D grid consisting of $m \times n \times o$ hexahedral unit-

cells as Figure 6(4) shows Additionally, the hexahedral organisation allows the research to utilise the vast collection of hexahedral-based unit topology in existing LCM research. In pursuing the objective of producing additive manufactured LCM at full-scale, the presented research develops macro-structured lattice with edge lengths of the unit-cells measuring at least 10mm. The scale of the unit-cell furthermore relates to the constraints of the robotics-enabled additive manufacturing process, which are discussed in Section 4.3.1.

3.3 General lattice cellular material design workflow

Given an initial hexahedral-like design volume, the steps for producing conformal lattice material are as follow:

- create initial hexahedra-like design volume with tri-parameter configuration

- generate normalised increments for subdividing the design volume

- interpolate the 3-D grid points corresponding to subdivision increments

- assemble unit-cells from 3-D grid points

- construct truss topology within each unit-cell.

Figure 6　Data organisation of LCM and corresponding geometric entities – showing the LCM design volume's (1) boundary surfaces; (2) primary axes; (3) primary surface planes and the (i) normalised parameterisation for any point within design volume as related to (1–2); (4) unit-cell organisation; and (5) tri-parameter grid point organisation and (ii) corresponding grid points for any given unit-cell
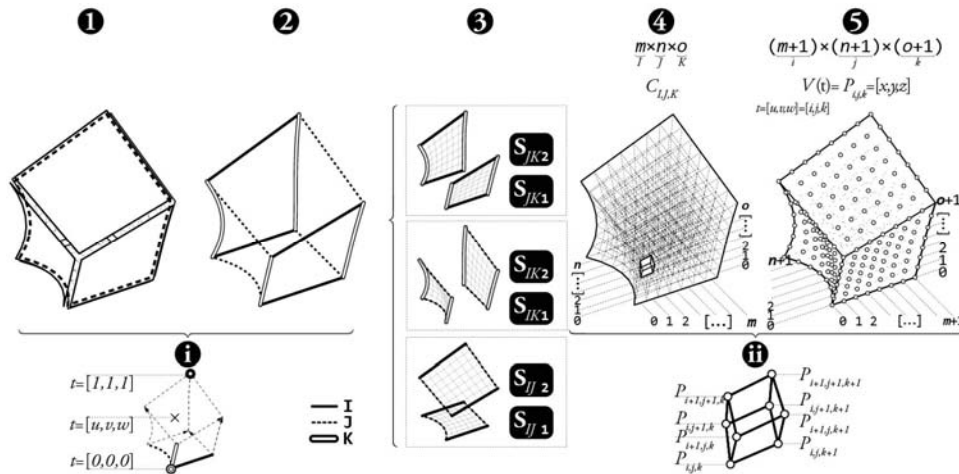

3.3.1 Design volume initialisation and tri-parameter configuration

The process for LCM generation begins with the initialisation of a parametrically generated hexahedral-like volume (Figure 6(1)). Figure 6(1A) shows the application of the tri-parameter organisation, whereby the hexahedra-like geometry creates a unique tri-parameter warped space defined by 3 primary axis-clusters of *I*, *J* and *K* (Figure 6(2)), and 3 pair of primary surface (*IJ*, *IK*, and *JK*) derived from the 6 surfaces composing the

design volume (Figure 6(3)). Any internal coordinate $P = [x, y, z]$ within the volume may be located by the normalised parameters of $t = [u, v, w]$ using the original formula $V(t)$, where $V(t) = P$ and $u, v, w \in \mathbb{R}$, have intervals of $[0, 1]$, and correspond to interpolated positions along the volume's unique I, J, and K axes (see Figure 5). Figure 7 and equation (1) demonstrate this original formula – each point is essentially the average of three points independently interpolated between the three pair of primary surfaces.

Figure 7   Tri-parameter interpolation of internal coordinate within a design volume
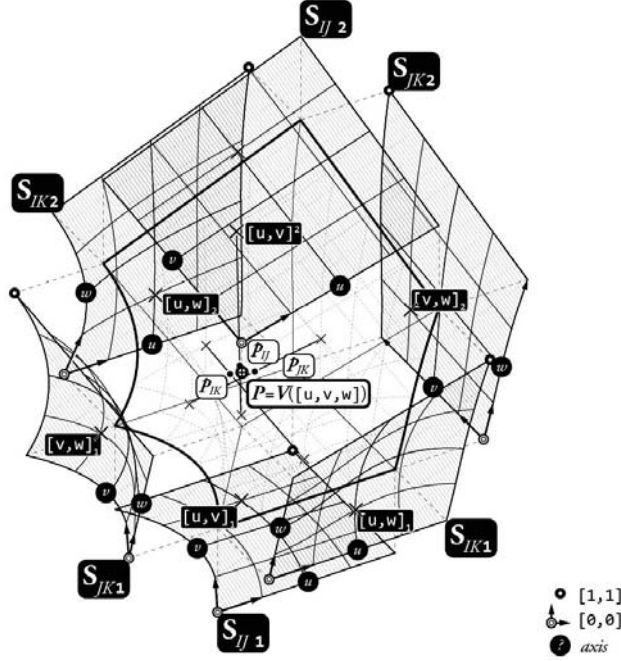
$$V([u,v,w]) = \frac{p_{ij}[u,v,w] + \boldsymbol{p}_{ik}[u,v,w] + \boldsymbol{p}_{jk}[u,v,w]}{3} \tag{1}$$

$$p_{IK}[u,v,w] = (1-v)\left(\boldsymbol{S}_{IK1}[u,w]\right) + (v)\left(\boldsymbol{S}_{IK2}[u,w]\right)$$

$$p_{JK}[u,v,w] = (1-u)\left(\boldsymbol{S}_{JK1}[v,w]\right) + (u)\left(\boldsymbol{S}_{JK2}[v,w]\right)$$

$$p_{IJ}[u,v,w] = (1-w)\left(\boldsymbol{S}_{IJ1}[u,v]\right) + (w)\left(\boldsymbol{S}_{IJ2}[u,v]\right)$$

$$i, j, k \in (0,1)$$

### 3.3.2   Volume subdivision and unit-cell construction

The $m \times n \times o$ unit-cells partitioning the design volume (Figure 6(4)), which is indexed as $[I, J, K]$, is constructed from a set of $(m + 1) \times (n + 1) \times (o + 1)$ coordinate points $P_{i,j,k}$ interpolated from a set of corresponding parameter points of $t_{i,j,k} = [u, v, w]$ (Figure 6(5)). Thus, each unit-cell at $[I, J, K]$ is defined by eight points consisting of $[P_{i,j,k}, P_{i+1,j,k}, P_{i+1,j+1,k}, P_{i,j+1,k}, P_{i,j,k+1}, P_{i+1,j,k+1}, P_{i+1,j+1,k+1}, P_{i,j+1,k+1}]$ (Figure 6(6)). The parameter points are in turn generated according to the normalised spacing increments

for each cell, which is conventionally set as [1/*m*, 1/*n*, 1/*o*] in conformal LCM generation prioritising even unit-cell distribution. The research proposed here similarly adopts this uniform parameterised spacing plan to construct the initial grid however, novel techniques for varying the internal density were developed and discussed at a later section.

3.3.3 Unit-cell module typology

Constructed within each unit-cell is the selected unit-cell module. This project uses the octet-truss as the unit-cell topology (Figure 8(1)). Originally designed by Buckminister Fuller for architectural application (Fuller, 1961), the octet-truss module has high structural efficiency, and variations of its configuration has widely been adopted in both conventional architectural construction and in robotics-enabled additive manufactured LCM applications. An octet-truss-based LCM may be constructed by the stacking of octahedral (Figure 8(3)) or tetrahedral elements (Figure 8(5)). The configuration results in a structural system with an average nodal connectivity of $z = 12$ (Figure 8(6)) – a necessary and sufficient condition for the structural action of the LCM to be dominated by axial action, which has greater structural efficiency than bending-dominated LCM. Deshpande has experimentally and theoretically investigated the effective mechanical properties of the octet-truss lattice structured material – describing lattice LCM as a promising alternative to metallic foams in lightweight structures (Deshpande et al., 2001).

Figure 8 (1) Unit-cell topology of octet-truss; (2) contextualisation of octet-truss module within a $3 \times 3 \times 3$ LCM; construction of octet-truss lattice can be achieved by stacking of (3) octahedral; or (4)–(5) tetrahedral elements; and (6) connectivity at a typical octet-truss node
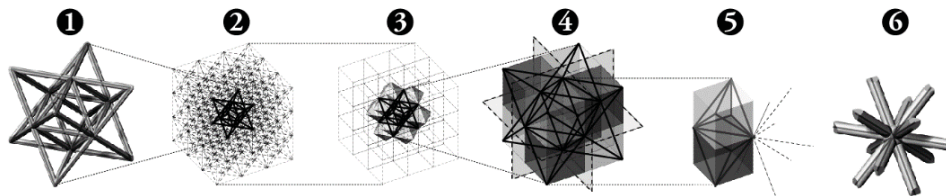
3.4 Software and hardware framework

3.4.1 Computational tools

To maximise the design relevance of the proposed framework among architects and engineers, the research uses popular 3D modelling tool Rhinoceros 3D, within the parametric visual programming language (VPL) environment of Grasshopper 3D (Robert McNeel & Associates, 2017). Finite element analyses (FEA) of the designed lattices were conducted using the plug-in Karamba (Preisinger, 2017). This research further utilises Goat (Rechenraum, 2017), which is an optimisation solver that relies on gradient-free optimisation algorithms found in the NLopt library (Johnson, 2017).

A combination of custom developed built-in Grasshopper components convert the optimised lattice geometries into robotic instructions, which is expressed in the KUKA robot language (KRL) – the proprietary language utilised by the KUKA light industrial

robot arm operating system (Braumann and Brell-Cokcan, 2011). The custom robotic programming allowed greater flexibility of the robotic control than commercial third-party software typically used for similar purposes. Continuing the use of Grasshopper 3D for fabrication planning, all stages of the design-fabrication process are integrated within the same CAD environment – thereby allowing seamless workflow transition from geometry generation to robotic programming.

3.4.2 *Additive manufacturing method and material selection*

The integrated software-hardware tool-chain proposed here addresses the AM technique of FDM, as the strength and ductility problem due to anisotropy is highly pronounced (Tam and Mueller, 2017). Additionally, FDM has commercial significance: it is cost-effective, widely used by designers, and produces parts that are relatively strong and durable (Gibson et al., 2010). Implementing FDM, the research has constructed a custom extrusion module that uses polyactic acid (PLA) – a material widely adopted in commercial desktop additive manufacturing platforms that has low toxicity, and can be extruded easily with limited geometrical distortion (Rafael, 2010).

4   Implementation I: computational generation, structural analysis, and optimisation

4.1   *Structural optimisation concepts*

This section describes the development of novel techniques suitable for the structural design characterisation and optimisation of geometrically complex LCM structures with a large number of design variables. The techniques are integrated within a fabrication-aware optimisation framework presented at the section's end.

4.1.1   *Overview of classical optimisation methods*

Structural optimisation is a classical subject in structural design whose purpose is to determine the modifications, which are expressed as design variables, to apply to an input structure in order to improve its performance, which is measured by an objective function – typically based on the minimisation of compliance, or the maximisation of stiffness (Achtziger, 1997; Bendsøe, 1995; Bendsøe and Sigmund, 2002; Svanberg, 1994; Rozvany et al., 1995). Most optimisation strategies follow a similar process consisting of the following steps (Mueller and Ochsendorf, 2015):

1   inputting of geometry, initialisation and domain specification

2   design variation

3   structural analyses, and computation of objective function

4   check for stopping criteria

5   conclusion, or repeating of process from (2).

Structural optimisation strategies are categorised by the structural design aspects varied to induce optimality, which include geometry, topology, and sizing. Geometry or shape

optimisation varies the geometry of the boundary elements enclosing a structural body, or the locations of individual characteristic nodes in the system (Figure 9(1.a)) (Allaire, 2002; Pedersen, 2000). By contrast, topology optimisation extracts a subset of elements from a pre-defined element set (Figure 9(b)) (Bendsøe and Sigmund, 2002). Finally, sizing optimisation involves modifying the optimal cross-section area for each elements within a fixed configuration (Figure 9(c)) (Bendsøe, 1995). Two classical methods conventionally used to implement optimisation are ground structures and homogenisation, which respectively characterise the structural design as a discrete structure of beam elements (Topping, 1993; Achtziger, 1997) (Figure 9(1)), or a continuum structure of cell elements with one or more holes (Bendsøe and Kikuchi, 1988) (Figure 9(2)). The determination of the optimal geometry and typology in both methods is transformed into a sizing problem, where optimisation considers respectively the sizing of the individual members, or the sizing of the small holes: elements with sizes below a defined threshold are eliminated.

4.1.2 Conventional optimisation techniques and lattice cellular material design

Classical optimisation strategies and methods are well-established; however, they have limited usefulness for the design and optimisation of LCM. Especially for the generation of 3-D volume, both topology and sizing optimisation – using either ground structures or homogenisation methods – would generally produce irregular systems (Figure 10) that are inconsistent with the periodic character of cellular material, and difficult to translate into fabrication instructions. Furthermore, it is well-known that the classical methods are computationally expensive, and can generate designs that are unusable, unnatural or unreasonable, such as grey area and disconnected structures (Lu and Kota, 2006) that cannot be materialised by AM (Leary et al., 2014; Doubrovski et al., 2011; Brackett et al., 2011).

Figure 9 Various optimisation methods and strategies applied for the (0) simply-supported design cases, which include optimisation by (a) geometry; (b) topology; and (c) sizing; via implementation of the (1) ground structures and (2) homogenisation methods
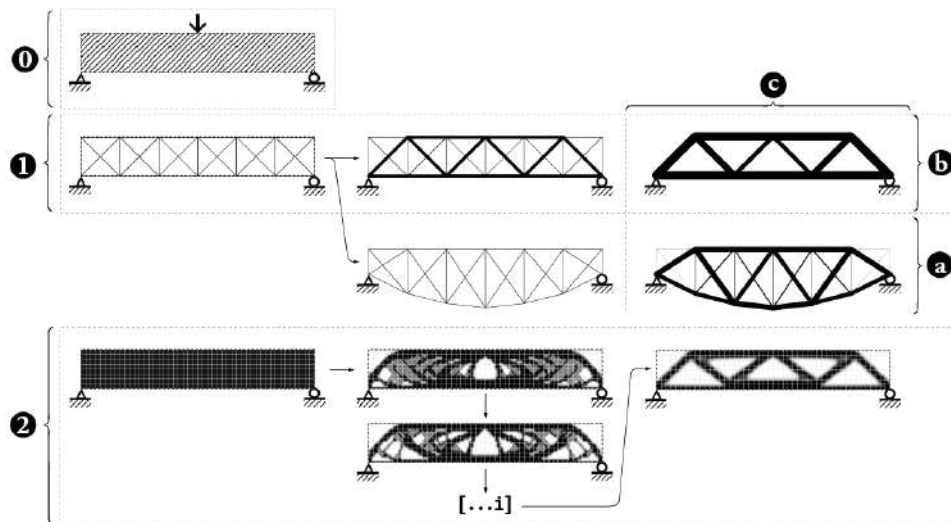
The review on optimisation suggests that the most appropriate optimisation strategy for designing AM-produced LCM is geometry optimisation, since the boundary volume of conformal LCM is a significant determinant of the LCM's form. Geometry optimisation of LCM furthermore maintains constant and regular element-node connectivity – thereby preserving the LCM's manufacturability. However, the properties of LCM, which are dense and complex structures defined by large number of control variables, present a number of unique challenges to the application of conventional design and optimisation approaches, which rely on the assignment of individual nodal coordinates defining the system's boundary as design variables. Such approaches generally require an unmanageably large number of design variables – leading to high computational expenditure and numerical instability. Usability of results is similarly exacerbated: individual variation introduces localised modification that are not guaranteed to conform to global geometrical characteristics. Additionally, the proliferation of design variables reduces the designer's capacity to control and configure the design space to affect meaningful and strategic variations.

Figure 10 Diagram illustrating numerical noises apparent in results obtained
for a design case featuring a (0) centrally loaded volume using the (1) ground structure method and (2) homogenisation method
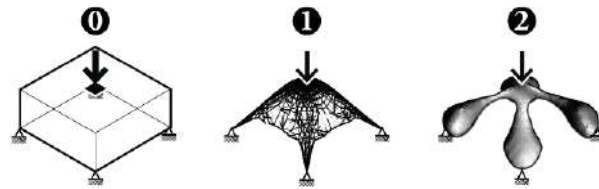
4.1.3 Strategies to simplify design problems with large variable space

Fundamentally, there is a need for new techniques to model structural designs with a large number of design variables and elements – techniques that can promote meaningful and usable variation in the design exploration of LCM structures, while simplifying the complexity in design characterisation. Research efforts to achieve this objective has generally followed three strategies – encompassing techniques that directly reduce the number of effective design variables, such as by (1) boundary representation (BREP) parameterisation (Figure 11(A.i.1)); and (2) variable mapping (Figure 11(A.i.2)); and (2) strategies that may combine these characterisation techniques to exploit the hierarchical complexity of LCM to allow the decoupling of design aspects (Figure 11(A.ii)).

1   Complex structures such as lattices may be constructed from an underlying surface or solid boundary representation models (BREP) by parameterisation using only a few design variables – leading to structures that are guaranteed to conform to the global geometrical characteristics of the underling BREP with minimal localised distortions. In this case, the design variable may for instance refer to the location or translation of the underlying geometry's control points. Structural design applications include both Mesh- (Shepherd and Richens, 2009; Bennett and Botkin, 1985) and NURBS-based approaches. NURBS-based approach in particular gained popularity because the format can be exchanged easily with computer-aided design (CAD) and computer-aided manufacturing (CAM) systems. Configurability is also

significant: NURBS-based modelling is numerically stable, and can be flexibly and intuitively modified to generate highly expressive and resolved geometries with only a few parameters. NURBS-based modelling has been incorporated in optimisation algorithms (Cervera and Trevelyan, 2005; Danhaive and Mueller, 2015; Wall et al., 2008) and specific project-based applications ranging from structural shell (Michalatos and Kaijima, 2014) to medical components (Clune et al., 2014).

2   Instead of directly reducing the number of control points used to characterise a structural design, the effective variable space can be reduced by developing mapping procedures that can compute the individual design vectors or values required for each design variable from functions or geometries defined with a smaller set *effective design variables*. Such functions or geometries may reference construction geometries used to model the structural design, or virtual geometries inserted by the designer, such as attractor objects. Parameters incorporated in the functions forming the basis of the mapping procedures may also be varied. The application has not been widely applied in structural engineering application, but is more often developed in computational architectural and visual design programming – informed by fundamental algorithms outlined in the works of Reas et al. (2007) and Shiffman (2015), where relevant approaches include the adoption of attraction and diffusion as a mechanism in force- and particle-inspired methods (Shiffman et al., 2012).

3   Directly related to the properties of periodic frame structures are methods that exploit the hierarchical complexity of LCM organisation to simplify the characterisation of the structural system – an organisation that can be conceived in terms of its geometry, subdivision, unit-cell module topology and member sizing. A fundamental benefit of the approach is that it allows the decoupling of variables characterising various structural design aspects – providing greater freedom and control for designer to achieve targeted variation, as seen in Figure 11(A.ii). Similar research has been pursued by Nguyen et al. (2012), who developed a framework for individual unit-cell typology selection for LCM, and by Chang (2010), who expanded the research to include member sizing. The hierarchical complexity of LCM also lends organisation for reduced modelling approaches, as typified in methods by Johnston et al.'s (2006) and Tam et al.'s (2017b) that consider each unit-cell, rather than the individual struts, as discrete FEA unit for analyses – thereby also reducing the total number of elements required for analysis.

4.1.4   *Limitations of existing strategies and optimisation objectives*

Although a large amount of research has been dedicated to simplifying the optimisation process for complex problems, few applications have been adopted specifically to enable the open-ended design exploration and generation of geometrically complex additive-manufactured LCM. In general, the various strategies identified are implemented in isolation: whereas BREP parameterisation methods typically focuses on global geometry variation and ignores the potential for multi-resolution parameterisation to alter the internal composition of LCM, conformal LCM research exploiting the hierarchical organisation of LCM have often ignored design aspects such as global geometry and internal density. While variable mapping offer potential application, its use in structural engineering has been limited. Geometrical limitation is also notable: existing implementations of similar modelling strategies in optimisation are applied to simple

surface-based design volume featuring large degree of planarity and constant thickness. Finally, most methods are generally agnostic to the requirements of fabrication.

In response to these limitations and opportunities, this research develops a fabrication-aware design optimisation workflow for generating complexly formed LCM with large variable using a collection of original computational techniques referred to as *GMT*. These techniques are specifically devised to exploit the unique geometric properties and hierarchical complexity of LCM, in order to enable a fuller exploration of the LCM design space that can be strategically and intuitively configured by designers – achieving complex geometric variations to both the geometric boundary and internal material distribution of LCM design while reducing the number of design variables and maintaining manufacturability.

Figure 11   Strategies for simplifying the characterisation of problems with large design variable set: (i) methods for reducing the number of effective design variables, such as (1) BREP parameterisation and (2) variable mapping and (ii) combination methods that take advantage of the (3) hierarchical complexity of LCM, such as internal variation in (a) density and (b) unit-cell module topology
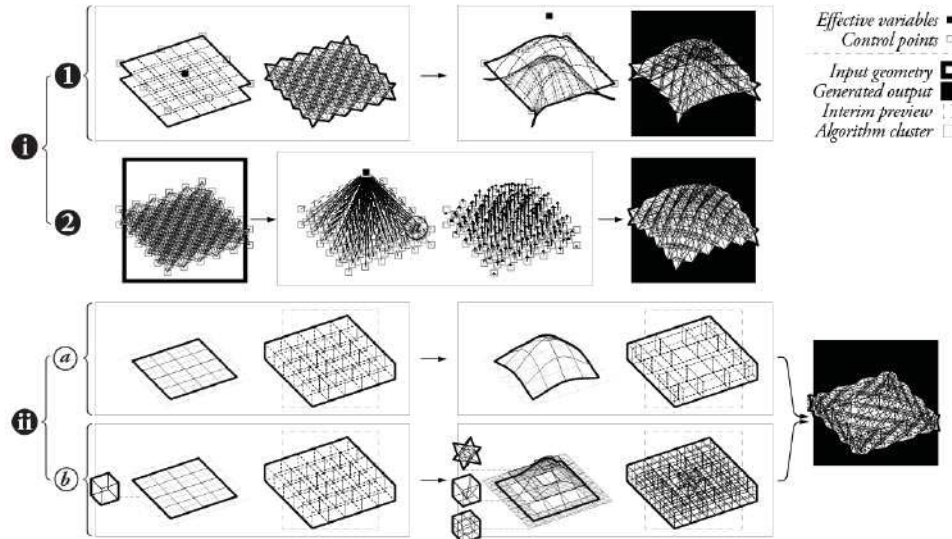
4.1.5 Motivating example

To motivate the research objective to simplify the complexity of the optimisation process, the classic cantilever optimisation problem is re-implemented on a basic rectangular parallelepiped LCM block. Both strategies rely on the minimisation of normalised strain energy and apply a vector translation to each interior node: whereas the first approach assigns an independent design variable for each node, the second approach requires only one effective design variable – following the variable mapping strategy explained in Section 4.1.3, and expanded in Section 4.2.1. Table 1 illustrates the efficacy of GMT in achieving comparably optimal structures with dramatically improved geometrical consistency. Furthermore, computational requirement is greatly reduced: a 98% and 40% decrease in respectively the number of effective design variables and iteration is achievable.

Table 1 Comparing the optimisation setup attributes and outcomes between conventional characterisation methods and the proposed GMT methods

	Conventional technique	*Global morphing methods*
Nodes modified	76	
Effective design variables	76	1
Best result: strain energy	36.9	37.3
Iterations	1500	600

4.2 Proposed optimisation framework

This subsection describes the subset of GMT techniques, called primitives, incorporated into the LCM generation framework to simplify the characterisation and modelling of the design domain and variables. The techniques presented here implement the strategy of *variable mapping*; they are applied either incorporated to the geometry initialisation stage, or within the design variation stage, as described in Section 4.1.

4.2.1 Primitives: global morphing techniques for density variation

Conformal lattice generation methods are generally developed with the goal of achieving a field of geometrically similar and equivalently sized unit-cells that varies gradually and uniformly within the LCM's boundary surface or volume. The preference for geometric uniformity, however, enforces an inversely proportional relationship between density and depth of the global geometry that is not always structurally desirable, as the cell sizes will expand and compress along with the global geometry – leading to potentially inefficient structures in cases where it may be preferable to have both greater element concentration and geometric depth.

Contour spacing variation, which is shown in Figure 12, is a technique incorporated into the geometry initialisation stage for decoupling the control of the density of unit-cells and the boundary geometry of a LCM design. More precisely, the individual parameters defining the spacing increment of unit-cells along each of the tri-parameterised hexahedral-like volume's three principle axes are modelled using NURBS-based polynomial functions. During optimisation, the coordinate values of the control points defining these functions are iteratively varied. Following each adjustment, the NURBS-based function is solved to obtain the precise normalised increment value used to interpolate the 3-D grid points used to construct the LCM's unit cells Figure 12(2).

To enable greater variation in the magnitude, position, scale, and concentration of the density variation achievable within the LCM, a set of techniques known as vector-based morphing can be incorporated into the Variation stage. These techniques, which belong to a class of techniques termed *object-based morphing*, inserts virtual geometric objects into the model space to exert field of influences that can be interpolated at any point of the model space to derive the design vector required for each control node characterising the structural system. The virtual geometry, which may be a 1-D point, 2-/3-D line or curve, or a 3-D surface, is first inserted into the model space in its initial state and modified via

optimisation of its control points to its morphed state (Figure 13(1)). The differences between the object at their two states define a vector field that can then be mapped to each of the control nodes of the structures according to user-defined mathematical formulations – producing the design vectors required to morph the LCM (Figure 13(2)).

Figure 12 Global morphing techniques #1: contour spacing variation – showing the (1) pre-morphed LCM and the (2) morphed LCM following modifications on the control points of the NURBS defining the unit-cells' spacing
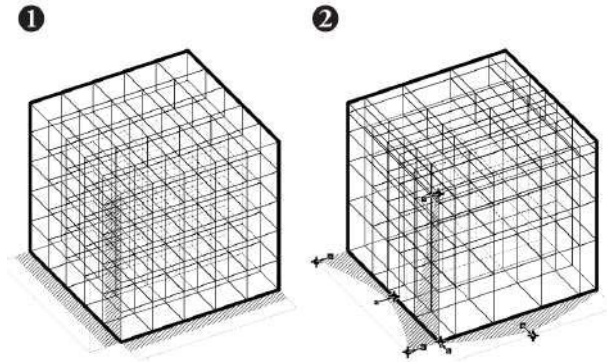
Figure 13 Global morphing technique #2: Object-based vector-defined morphing – showing the (1) introduction of virtual objects, which are modified to create a vector field that (2) generates the design vectors required for each node within the lattice (see online version for colours)
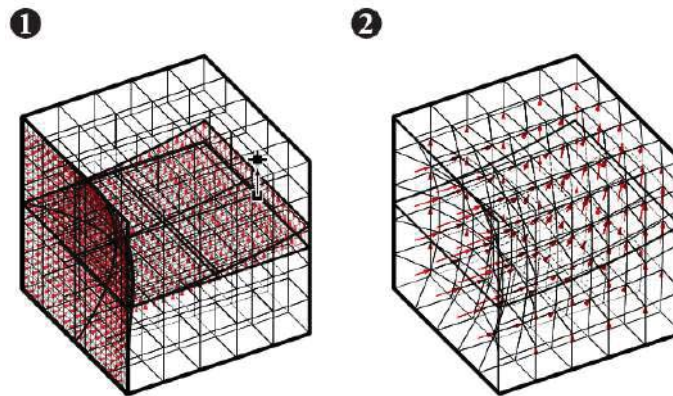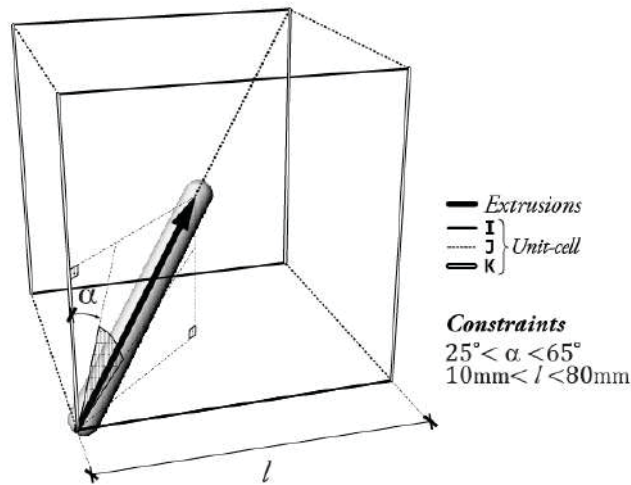

4.3   Fabrication-aware optimisation

4.3.1   Characterisation of fabrication limitations

To study the constraints of the robotics enabled fabrication process, unit-cells were extruded at a variety of dimension and aspect ratios. Considering both the relative ease of the extrusion process, and the quality of the fabricated specimen, the empirical observations reveals that the limitations of the fabrication process can be expressed in terms of the printable length and inclination angle ranges of members (Figure 14) – similar to the characterisation of fabrication constraints typically adopted in design

optimisation methods developed for commercial FDM methods (Leary et al., 2013, 2014; Hague et al., 2003; Chang and Tang, 2001).

Applied to robotic fabrication, both criteria accounts for the potential collision between the custom extrusion module and the members, which typically occurs when an edge length of a unit-cell is below 0.01 m, or when the angle between a *supported* or *unsupported chain* segment (tool-path decomposition types that are explained at Section 5.4.1) and its containing unit-cell's *K*-axis is outside of the 25°–65° range. The member length range also considers the maximum length of filament that can be cantilevered without significant creep deformation during extrusion, which occurs when the length of a segment exceeds 0.08m. To balance the trade-off between minimising robotic collision and creep deformation, a targeted average unit-cell size of 0.04 m in edge length was set. Finally, the dimension of the LCM is constrained by the printable volume, which refers to a contiguous volume of space in front of the robot where minimal robotic move and joint limitations are expected – measuring approximately 0.75 m in length and 0.25 in both width and height.

Figure 14 Fabrication constraints expressed as ideal length and inclination angle range

4.3.2 Objective function and optimisation framework

Incorporating the GMT, the fabrication-aware optimisation of LCM is formulated as a single objective function with soft constraints, where constraint violations are included as penalties in the objective function. The objective, which is formulated in equation (2), is the minimisation of strain energy normalised by the total length of members, otherwise known as the maximisation of stiffness (Bendsøe and Sigmund, 2002; Rozvany et al., 1995; Svanberg, 1994). In the presented formulation, $X_1, \dots X_N$ refer to all design variables, $P(X_1, \dots X_N)$ to the penalty parameters for all constraints in the form of $\delta(X_1, \dots X_N) < \delta_{max}$, and $U_i(e)$ and l_i respectively to the strain energy and length of beam elements i within the system of m elements. Structural performance and manufacturability are considered through δS, δL and δA, which correspond respectively to the members buckling within a factor of safety, members with length outside of the

printable range and nodes with elements intersecting at angles outside of the allowable inclination range.

The maximum aggregate percentage allowance, and the penalty constant, which are respectively represented by $\delta_{\max}$ and C_p, are arbitrarily defined by the designers.

$$\min_{(\underline{X})} J\left(\underline{X}\right) = \sum_{i=1}^{m} U_i^{(e)}\left(\underline{X}\right) \times l_i\left(\underline{X}\right) + P\left(\underline{X}\right)$$

$$U_i^{(e)}(\underline{X}) = EI \int_0^{l_i} \frac{1}{2}\left(\frac{d^2 v}{dx^2}\right)^2 dx$$

$$P\left(\underline{X}\right) = \begin{cases} 0, & |\delta_S + \delta_L + \delta_A < \delta^* \\ c_p, & |\delta_S + \delta_L + \delta_A \geq \delta^* \end{cases} \tag{2}$$

$$\delta_S = \frac{m_{\text{buckling}}}{m} \; ; \delta_L = \frac{m_{\text{bad length}}}{m} ; \delta_A = \frac{n_{\text{bad angle}}}{n}$$

$$\underline{X} \in (-1,1)$$

Integrating the GMT and fabrication-aware optimisation framework with the LCM design generation, the process for generating optimally morphed conformal LCM, which was first introduced in Section 3.3, is revised to the following: (0) Initialise tri-parameter hexahedral-like volume; domain specification (1) Variation I: Morphing of NURBS-based surface boundaries; (2) Generate parameterised increment for subdividing the design volume; (3) Remapping of parameterised increment using *contour spacing variation*; (4) Interpolate points for 3-D grid construction; (5) Variation II: Morphing of 3-D grid points using various GMTs; (6) Create unit-cells; (7) Construct truss topology within each unit-cell; and (6) Geometric processing of lattice structure; (8) Structural analysis and evaluation of objective function output; (9) Continue optimisation by repeating process from (2), or terminate. The design and optimisation procedure concludes with the output of the generated LCM as centre-line geometries.

5   Implementation II: robotic planning and strategy

A formalisation of the procedures for converting centre-line LCM model into printing instructions is presented in this section, which encompasses new hardware design, and robotic programming strategies specifically considering the geometric configuration and properties of octet-truss-based LCM.

5.1   *General robotic workflow*

The typical fabrication workflow consists of the primary stages of (1) Initial import and sequencing of LCM geometry; (2) Robotic work-cell calibration and print positioning; (3) Geometric post-processing and conversion of LCM geometry into robotic path, and (4) Fabrication simulation and implementation. Specifically, the primary stages are further broken into the following sub-steps: (1.1) Import centre-line model of LCM; (1.2A) Grouping of LCM member elements into independent print programmes according to the layering of LCM along its K-axis; and the (1.2B) Clustering of LCM members of each programme into groups according to the octet-truss sequencing strategy

explained in Section 5.4.1; (2.1) Positioning of the printing platform; (2.2) Tool and printing surface calibration, which outputs coordinate data incorporated into robotic instruction; (3.1) Generation of tool-paths from the member groups, which incorporates (A) Approach and retraction sequences (Section 5.4.2); (B) Rule-based geometrical modification of centre-line geometry to improve printing quality (Section 5.4.2; Section 6.3.2); and (C) Corresponding robotic programming parameters and positioning data; (3.2) Simulation of robotic motion using KUKA Sim Pro, which is the official simulation software developed by KUKA; (3.3) Iterative correction and optimisation of robotic parameters; (4.1) Export of KRL code and execution of program on the KUKA; and finally (4.2) Robotic fabrication using the hardware equipment described in Section 5.2.

5.2   Robotic fabrication setup

Robotics-enabled additive manufacturing was enabled by the use of the KUKA KR6 R900 SIXX (KR AGILUS) 6-axis industrial robot (KUKA AG, 2017). Figure 15 illustrates the fabrication work space, where the KUKA is centrally located inside a work-cell. The customised extrusion module is connected to the KUKA with a pneumatically actuated tool-changer. Clamped in the centre of the worktable is a bed of polyurethane foam covered by a sheet of taped paper, which acts as both the printing platform and the safety protecting the extruder module in case of collision due to calibration errors.

Figure 15 Photograph of robotic fabrication work-cell
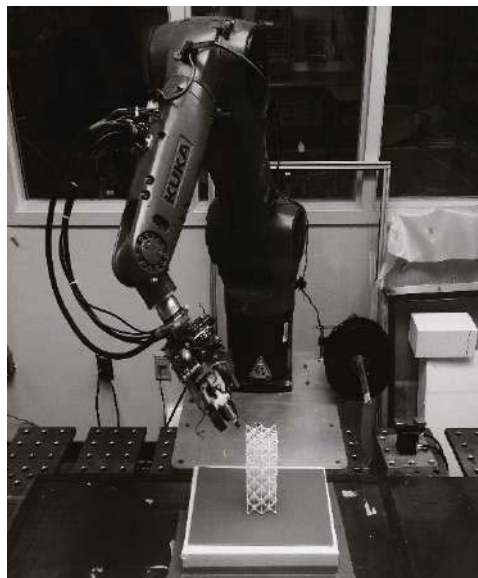
5.3   Custom extrusion module

Construction of a 3D printing end effector capable of extruding freestanding structures required a combination of custom hardware, electronics, and cooling, as illustrated in Figure 16.

Figure 16 Schematic layout of the custom-developed extrusion module for producing LCM
             (see online version for colours)
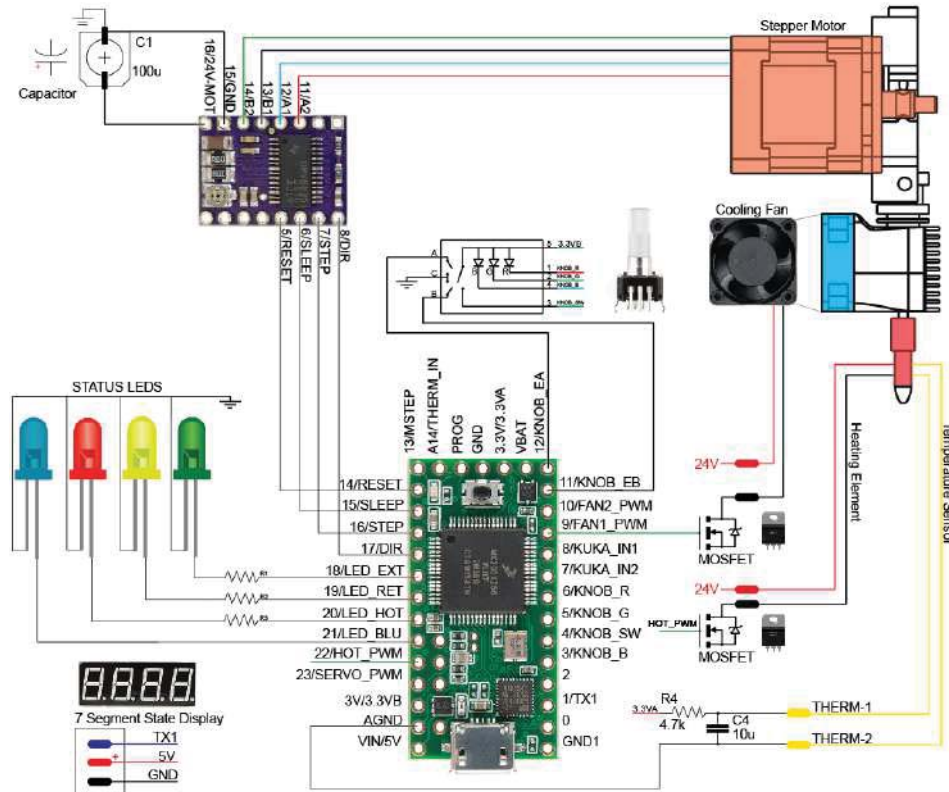
The initial implementation presented in this paper relies on a single brass nozzle for filament extrusion. Thus, the cross section of all members composing the LCM parts presented in this research are fixed in diameter. While the nozzle restriction precludes the opportunities for sizing optimisation, which limits the achievable structural efficiency in produced parts, the restriction also simplifies the research methodology – enabling the authors to reduce the complexity in hardware design and focus specifically on the structural benefits of global and internal geometry variation.

   To ensure that the extruded members are capable of holding their form while cooling and transferring forces through the structure, a nozzle with a diameter larger than those used in commercial desktop 3D printers was selected–measuring at 1.2 mm in diameter. The nozzle's exterior was machined down to a slimmer profile for manoeuvrability, and wrapped with a nichrome wire heating element capable of quickly heating the unit to 200–300°C. A NEMA17 stepper with a toothed drive gear was mounted directly above the aluminium heatsink in order to feed the 1.75 mm PLA filament into the heated nozzle.

   Between the KUKA arm and extruder hardware, a custom electronics board powered by a Teensy 3.1 microcontroller was responsible for regulating the extruder's temperature and extrusion rate. A tuned PID loop was developed to regulate the nozzle at a stable temperature regardless of environmental conditions using feedback from a thermistor

temperature sensor. The extrusion rate of the unit was controlled by a DRV8825 stepper motor driver, which was in turn controlled by the microcontroller. Both the temperature and extrusion rate could be fine-tuned on the device via a rotary encoder control knob and seven-segment display to show the status. To control extrusion directly from the robot arm's KRL code, one digital output from the arm was wired as input to the microcontroller such that a logic HIGH would extrude material at the set speed, and a logic LOW would stop extrusion. On a HIGH-to-LOW transition, a predetermined retraction sequence would be executed in order to retract the filament slightly, reduce pressure in the nozzle, and prevent residual filament flow while the robot arm moved between joints of the LCM structure.

5.4 *Robotic programming for materialisation of cellular lattice material*

5.4.1 *Clustering and sequencing of octet-truss-based lattice cellular material*

The primary objective of the robotic programming and motion planning is to determine a topologically-aware and fabrication-efficient sequencing strategy to link the large number of independent member segments of the LCM geometry into a limited number of clusters, or chains, which are relatively uninterrupted robotic extrusions of a series of member segments. Each LCM geometry is decomposed into a number of independent *print programmes*, while each programme consists of multiple *chains*.

The tri-parameter 3-D grid organisation of LCM permits the decomposition of a given LCM volume into independent print programmes corresponding to the each layer of unit-cells along the LCM's K-axis. To avoid member collision during the extrusion process, each layer of unit-cell modules, which consists essentially of X-shaped braces, is further subdivided into two half-layers of V-shaped braces (Figure 17(2)) – a half-layer of V-shaped braces (Figure 17(3-B)) supported by a half-layer of inverted ones (Figure 17(3-A)) – that are each in turn connected to a base layer consisting of diagonal grid members. Following the layer-based subdivision, the members in each half-layer are clustered according to their alignment with the design volume's three primary surface-planes of *IK*, *JK*, and *IJ*, as Figure 18(1) illustrates. The clustering results in the formation of independent and continuous zigzag-like chains of joined V-shaped brace elements organised under three fabrication-informed categories (Figure 18(3)). In the order of the printing sequence (Figure 18(2)), these categories include (1) *base chains*; (2) *unsupported chains*; and (3) *supported chains*.

As Figure 18 (1-'IJ'; 2-'Base chain', 3-'TP$_{IJ,B1-2}$') shows, *base chains* consists entirely of the diagonal-grid like members on the IJ surface-plane: they are printed either directly on the printing bed, or as members spanning the existing nodes of both the *supported* and *unsupported chains* members. As the first set of elements to be printed for each layer, *base chain* members may be printed with minimal interfering obstructions from pre-existing elements. The completion of *base chain* elements are followed by the printing of *unsupported chains*, which consists of elements oriented to both the IK and JK surface planes (Figure 18(1); 2-'Unsupported chain'). As suggested by its naming, unsupported chain members are partially printed as cantilever mid-air (Figure 18(3)-'TP$_{IK,U1-2}$ and TP$_{JK,U1}$'). Once the unsupported chains have been printed, the final group of tool-paths, which are called supported chains (Figure 18(2)-'Supported chain'; 3-'TP$_{IK,S1}$ and TP$_{JK,S1}$'), are extruded in between the nodes created by the unsupported chains – consisting also of members oriented on the IK and JK surface planes. In general, the

individual continuous zigzagging chains in each tool-path groups are sequenced according to proximity, and a general global direction as Figure 18(3) shows.

Figure 17 Decomposition of a (1) demonstrative 5 × 5 × 8 LCM into the (2) independent print programmes according to the layering of LCM along its *K*-axis. (ii) Each layer is further decomposed into two half-layers – as explained in detail in (3)
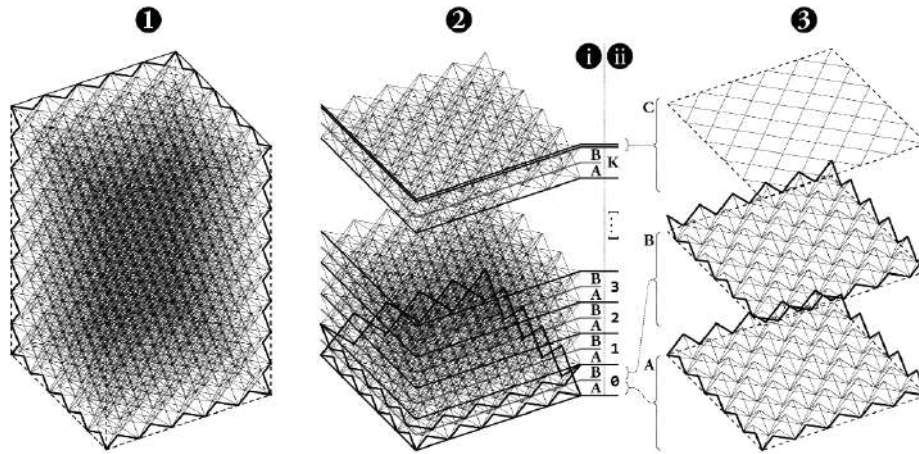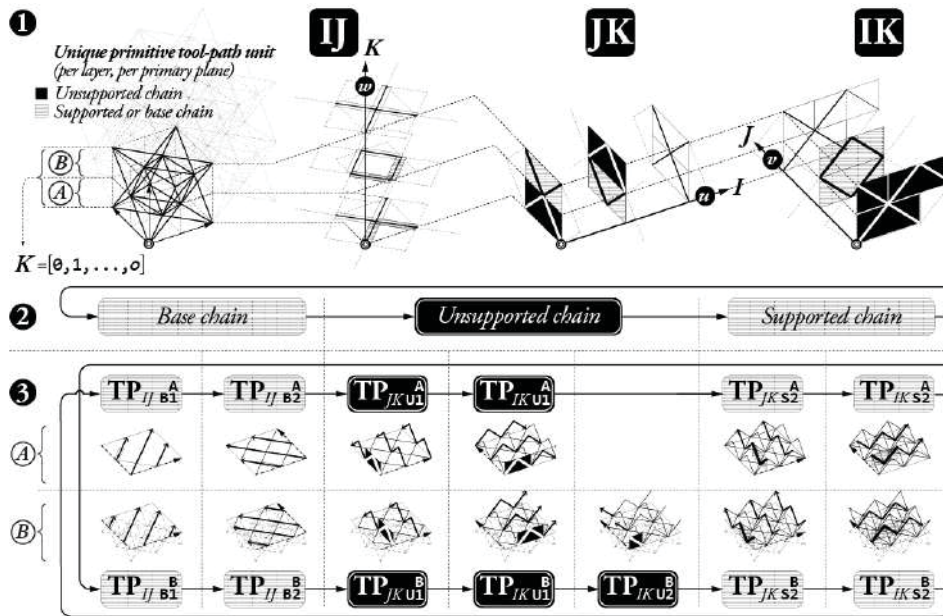

Figure 18 Decomposition of the octet-truss unit-cell topology at each of its three primary surface-planes into (1) primitive tool-path segments, which are (2-3) linked and sequenced in the LCM fabrication as *base*, *unsupported*, or *supported chains* – alternating between the two half-layers of (A) and (B)

The decomposition scheme outlined above offer a few fabrication advantages. Firstly, the V-shaped elements are linked efficiently and continuously as zigzagging tool-path – sharing similar advantages with the conventional FDM tool-path planning strategy of direction-parallel paths (Jin et al., 2013). The sequenced organisation reduces total print time by minimising the jump distance incurred due to the relocation of the extruder in between the extrusion of isolated chains, and the wait time required for repeated activation and deactivation of the extruder at the start and end of each independently printed member segment. Consequently, the strategy also minimises the structural and geometrical corruptions to the LCM print caused by the accumulation of residual filament flow incurred by the constant deactivation and reactivation of the extrusion module.

5.4.2 *Robotic and extrusion module programming parameters*

Having established the sequencing of the lattice member for print, the custom developed robotic programming tool converts the centre-line LCM geometry into move commands in the KRL format while inserting necessary commands to control the end-effector according to a number of extrusion module settings, joints configurations, and tool-path generation parameters. As explained in Table 2, these parameters may be altered to affect the filament quality. A demonstrative algorithm incorporating the fabrication mechanism and parameters for the printing of a simple chain is presented in Algorithm 1, which shows the prefacing and post-facing of each chain by large clearance and move operations, whereas the multiple V-shaped braces composing each chain are in turn broken into as extrusion of individual line segments each prefaced and post-faced with short pauses for temperature control.

For a typical chain, a point-to-point (PTP) movement is utilised within the initial approach and final return sequence respectively from and to the home position at the beginning and end of the print programme, and within the retraction and linking sequence during and between the printing of individual and independent chains (Line 1–2; 16–18 in Algorithm 1). Internal movement within each chain is subsequently achieved using linear (LIN) movement – with pauses (Table 2.W) incorporated upon the arrival of each constituent node of the chain to provide sufficient time for heating (Line 4) and cooling (Line 7–9) following respectively the activation and termination of the extruder at the start and end of each segment. Temperature control is especially critical in the printing of *unsupported chains*: since there are no nodes or platforms to support or connect these cantilevering extruded segments, additional time is provided to allow recently extruded heated thermoplastic to cool and harden – thereby minimising the sagging of the member when the filament is still flexible at the glass transition phase.

Geometrical post-processing of the centre-line lattice model is also incorporated into the robotic tool path to reduce the geometrical discrepancies between the model lattice geometry and the final printed geometry, and to reduce filament collision at the joints, since the original centre-line model did not consider material thickness. For instance, nozzle collision with existing nodes are avoided by programming the incoming nozzle to

reach a position that is slightly offset above the node, before the nozzle presses down, retract upward, and commence the extrusion of the subsequent member (Table 2.R; Line 8; 10). Globally, the potential discrepancies in nodal height due to deformation of the LCM is accounted for by offsetting the nodal positions in each K-layer according to a calibrated positive small Z distance. Figure 19 shows the implementation of the robotic programming strategy for an arbitrarily morphed LCM.

Table 2   Key robotic programming parameters and concepts

Key	Key parameter	Description
TAO	Tool axis orientation	Three categories of orientations are utilised during fabrication: (1) The highest material consistency and, by extension, aesthetic and structural performance is achieved when the extruder module nozzle is oriented in parallel alignment to the member being extruded. In the majority of cases where joint rotational and collision prohibit oriented material deposition, the nozzle is either (2) oriented in the axis perpendicular to the horizontal printing bed, or (3) alternative axes in rare circumstances where collision will be unavoidable using the first two type of alignments
MR	Move rate and travel rate	The robot's move rate, as defined by the rotation of the joints, is dynamically adjusted to enforce the maintenance of constant travel rate. The travel rate, which is currently set at 7 mm/s, refers to the travel distance of the extrusion nozzle over one unit of space as the filament-member is extruded
ER	Extrusion rate	The length of filament that the stepper motor is able to extrude per unit of time is currently set at 5 mm/s – a value deliberately set below the travel rate in order to pre-tension the filament, which reduces sagging of the recently extruded members due to heat and gravity
R	Mechanical retraction	Following the extrusion of a filament-member at the position of the node-joint, the robot is retracted vertically upward in the axis perpendicular to the printing plane for several functions: (1, or R.C) To provide clearance for avoiding collision during initial approach to the first point of the beginning of a continuous chain; (2, or R.D) To adjust for deflection, or to provide clearance to minimise filament collision; and (3) R.T remove the heat source of the nozzle to enable cooling
W	Wait time	Wait time is provided for in order to: (1, or W.H) allow time for filament to be reheated; and (2, or W.C) achieve cooling, which is dependent on the member type being printed, and is controlled by the duration of pause following the completion of a filament-member at the position of the joint
CA	Extruder and cooling activation	Activation/ deactivation of the extruder, and the cooling fan are respectively enabled by the declarations in the KRL code of 'Extrude = True/False' and 'Cooling = True/False'
EA	Extrusion activation timing	To mitigate the loss of filament due to a residual pressure gradient across the nozzle and to ensure the production of normalised flow at the start of new chains, the filament is retracted immediately after the end of a chain to break connection with the previous filament, and extruded again just prior to recommencing print for the following chain

Algorithm 1 Demonstrative KRL code showing the fabrication of an unsupported V-segment

Algorithm	*Notes and parameters*
#First Chain	
1: PTP {X 0,Y 50,Z 30,A 90,B 90,C 90}	{Table 2.R-C} Clearance
2: PTP {X 0,Y 50,Z 0,A 90,B 90,C 90}	**Start point**
3: EXTRUDE = TRUE	{Table 2.A-EA} *Start Print*
4: WAIT SEC 1.5	{Table 2.W-H} Heating 1
5: LIN {X 0,Y 25,Z 25,A 90,B 90,C 90}C_DIS	**Cantilevered point**
6: EXTRUDE = FALSE	{Table 2.A-EA} *Stop Print*
7: WAIT SEC 3	{Table 2.W-C} Cooling 1A
8: LIN_REL {z 0.5}	{Table 2.R-T} Retract 1A
9: WAIT SEC 10	{Table 2.W-C} Cooling 1B
10: LIN_REL {z 5}	{Table 2.R-D} Retract 1B
11: EXTRUDE = TRUE	{Table 2.A-EA} *Start Print*
12: WAIT SEC 2.5	{Table 2.W-H2} Heating 2
13: LIN {X 0,Y 0,Z 0,A 90,B 90,C 90} C_DIS	**Final point**
14: EXTRUDE = FALSE	{Table 2.A-EA} *Stop Print*
15: WAIT SEC 2	{Table 2.W-C} Cooling 2
16: PTP {X 0,Y 0,Z 26,A 90,B 90,C 90}	{Table 2.R-C} Clearance
#Second Chain	
17: PTP {X 50,Y 50,Z 30,A 90,B 90,C 90}	{Table 2.R-C} Clearance
18: PTP {X 50,Y 50,Z 0,A 90,B 90,C 90}	**Start point**
[...] **repeat**	

Figure 19 Photograph of an arbitrarily morphed LCM produced using the initial fabrication method
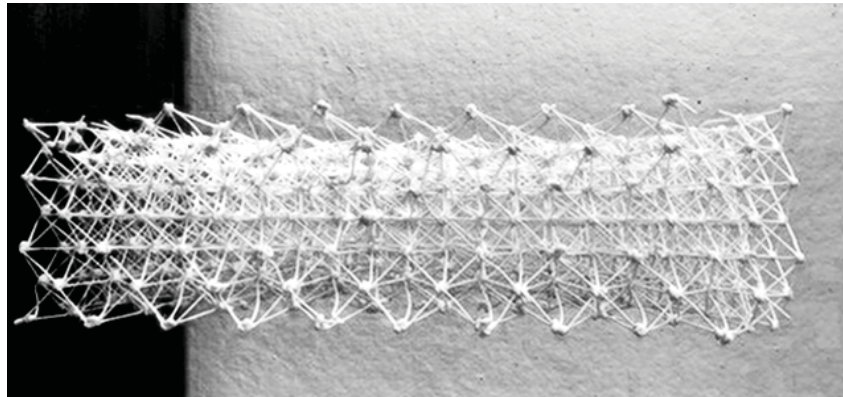
6 Implementation III: fabrication design and calibration

This section covers the extensive load testing and qualitative evaluation that were conducted on the specimen produced using the initial robotic implementation. Having analysed the initial results, mechanisms for achieving improvements to the structural

performance and geometrical fidelity of artefacts were proposed and developed – leading to a revised implementation that is evaluated at the section's conclusion.

6.1 Design of test specimen

The feedback-based experimental procedure were conducted using the standardised regular LCM block specified in Figure 20; it is neither optimised nor processed. As illustrated, the LCM is simply supported and loaded with one downward point load at mid-span on the topmost surface. The printed structures measures approximately 180 mm in length, 65 mm in width, and 58 mm in depth – with an average internal member diameter of approximately 1.2 mm.

Figure 20 Standardised LCM blocks used for testing in Implementation III
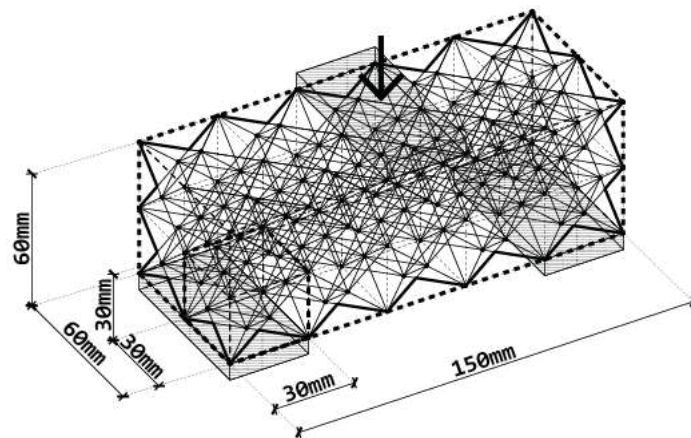
6.2 Initial implementation: qualitative and experimental evaluation

The initial implementation of the lattice material framework was largely successful at producing integral and connected LCM, as Figure 21(1) shows. However, two recurring geometrical characteristics affecting both the members and joints of the LCM were identified. Figure 21(2) and Figure 22(3.ii) shows the noticeable creep deformation along the length of the LCM members, with the deformation especially severe for the unsupported chain member segments – occurring at mid-span, and near the print end of the members. Under loading, such deflections can lead to bending stress that not only reduce the LCM's overall strength capacity, but increases the LCM members' susceptibility to buckling. Imperfection is similarly observed in the connection of the members at the joints, where the connection between the different continuously printed member classes are evidently weakened due to a reduction and tapering of cross section area nearing connection nodes, which can further diminish the strength capacity of the LCM.

Structural load testing on the initial lattice material specimen largely corroborated with the assessment above; with an average yield load-to-weight ratio of 230 in the four specimen tested, the initial lattice material is 67% weaker than the finite element analysis (FEA) prediction using the input LCM centre-line geometry. Additionally, as Figure 22(3.i) shows, delamination of members from the joints is pervasive – thereby

precluding the full utilisation of the members' capacity, and introducing unpredictability to the mechanical behaviour of the LCM, which is evident in the multiple instance of localised failures occurring during the linear elastic state of the LCM as it was loaded (Figure 22(1)).

The evaluation reveals large geometrical and material inconsistencies in specimens produced using the initial method, which include inadequate bonding of the filament at the connections, and excessive creep deformation of members during extrusion. Since the timing of the extrusion module and the robotic arm with respect to the temperature profile of the extrusions are key determinants of the overall mechanical properties of the LCM, the experimental procedure presented here focuses on the iterative calibration of the extrusion and robotic programming speed parameters, and developed geometrical processing techniques for improving the interfaces of bonding layers. Both a video camcorder and a thermal imaging camera were utilised for documenting the extrusion process.

Figure 21 Photographs showing (1) fabrication of the standardised LCM block using the initial method and (2) the produced LCM block in closeup
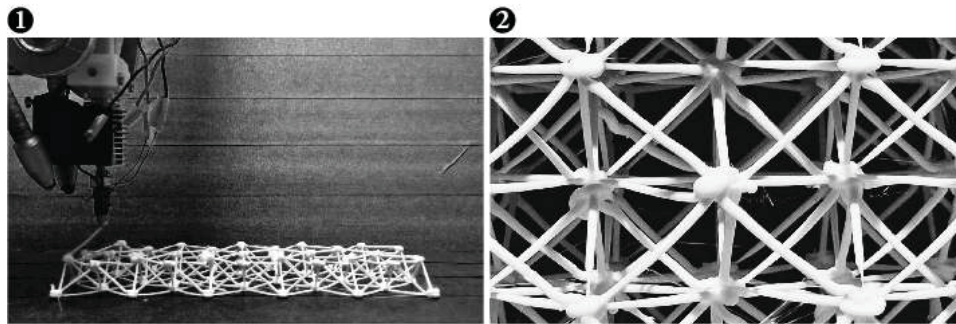
Figure 22 Documentation of load testing conducted on specimen produced using the initial fabrication method: (1) unpredictable structural behaviour at the linear elastic state; (2) load testing setup; and (3) common issues identified, which include (i) joint delamination during load testing; and (ii) creep deformation of member during printing
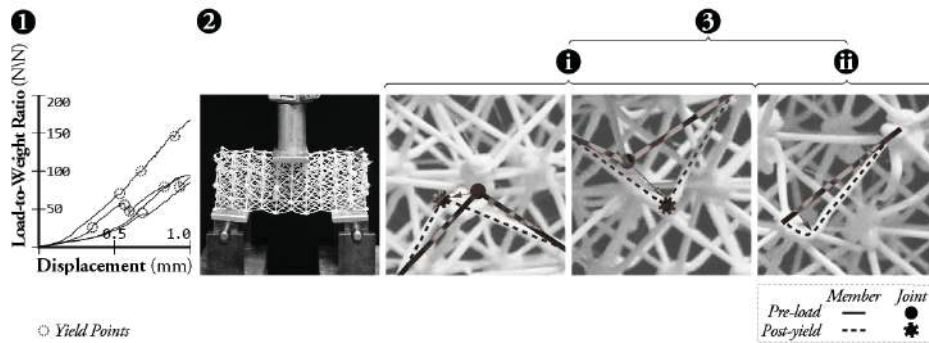
6.3 Fabrication process improvement

6.3.1 Reducing creep deformation by thermal-imaging-enabled calibration

The occurrence of creep deformation suggests that the filament may be extruded at a rate that is higher than optimal for the given robotic travel speed, and that both speed parameters do not allow sufficient time for the filament to cool (Table 2.ER and Table 2.MR). While PLA is heated to a temperature of 220°C, empirical evidence has demonstrated that material solidification in PLA occurs only when the temperature of the filament is below 80°C (MatterHackers, 2013). However, thermal imaging records of the initial method shows that the printing of a subsequent member has typically commenced even when the temperature of the preceding member remains well above the PLA's glass transition temperature of 60–65°C (Figure 23); consequently, viscous flow mechanism at this temperature range render the filament vulnerable to creep deformation both by its self-weight, and by the extruder's motion. The geometric corruption is especially problematic in the printing of *unsupported chain* members, which experience greater distortions as they are printed as cantilevering members in mid-air. Since the vertical discrepancy in height caused by the internal sagging of the members accumulates with each layer of unit-cells in the LCM that are printed, the improper calibration of move and extrusion rate produces significant global geometrical inaccuracies.

Figure 23 Temperature profile of the end of a recently extruded member as the printing of the subsequent member commences (see online version for colours)

The revised implementation reduces these inaccuracies by providing sufficient time for the unsupported member filament to cool. There is, however, a large trade-off between fabrication speed and quality: with the filament requiring on average 12 seconds to cool, as Figure 24(2) shows, material cooling by passive room ventilation will augment the total required printing time, which reduces the fabrication efficiency. To achieve material cooling more expediently, a new electronic fan operated system was setup to utilise controlled blasts from the compressed air – running air from the end effector attachment ring and through an air regulator, and then targeting the extruded plastic using a directed nozzle (Table 2.CA). The new method reduces the required cooling time to only 5 seconds – thereby improving the material quality of extruded filament with limited reduction to printing efficiency.

Figure 24 Image sequence documenting the change in temperature profile of a recently extruded
member by (1) standard video recording and (2) thermal-image camera – showing that a
total of 12 seconds is required to ensure sufficient cooling in the member (see online
version for colours)
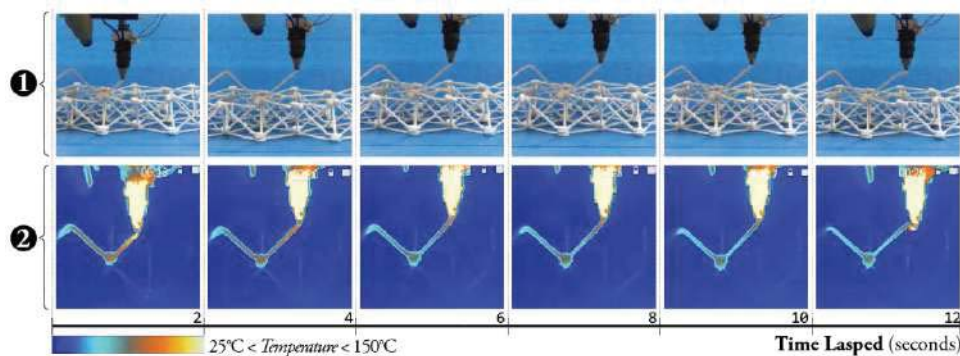
6.3.2 *Timing-calibrated rule-based tool-path modifications*

In octet-truss-based LCM, a joint is created by overlapping six layer of filament chains.
Bonding quality is dependent on the degree of completion of the bond formation process
between the filament layers composing the joints – a process for polymeric materials that
begins with (1) initial surface contact; followed by (2) neck growth between the filament,
which is called *sintering*; and ending with the (3) molecular diffusion and randomisation
at the interface of the contacting layers of filament, which is referred to as *healing*
(Sun et al., 2008). Whereas the bonding at the first stage is primarily mechanical and
frictional, and depends largely on the amount of overlap between contacting filament,
sintering and *healing* are respectively viscous flow mechanism (Narkis, 1979) and
molecular phenomenon driven by thermal energy of the extrusions, which can be affected
by time and temperature-related parameters of the extrusion process.

While both contact surface area and temperature are contributing factors to the bond
formation process, the algorithm for converting LCM centre-line geometries to robotic
commands in the initial implementation was developed largely with the objective
(1) to minimise the geometrical discrepancy between the modelled and printed LCM;
(2) to avoid filament collision at the joints; and (3) to expedite production. Thus,
modification to the LCM centre-line were limited to offsets accounting for material
thickness and creep deformation, whereas the extrusion timing was programmed to allow
the extruder to deposit filament material on top of an existing joint at a constant extrusion
speed with minimal interruptions, even if the interfacing filament may have already
cooled and solidified. Since the contact between the incoming and existing filaments are
greatly limited by these approaches, the bonding at the interfaces are often incomplete –
lacking both in contact area between the interfacing filaments, and in heat transfer from
the incoming extrusion to the existing joint to enable sintering and healing.

To promote better fusion of the interfacing filament, targeted contact between the
nozzle and the existing joints were incorporated in the revised fabrication method as
geometrical modifications of the tool-paths that combined timed mechanisms designed to
prolong the exposure of the existing printed joint to the incoming extruder's heated

nozzle. Informed by the research of Sun et al. (2008), who found intensified sintering and healing between interfacing filament layers with temperature above respectively the critical sintering temperature and glass transition temperature, the revised approach extrudes a supported chain segments until it connects to an existing joint; at this point, the extrusion rate is slowed, and the nozzle is pressed onto the existing joint for a duration determined through calibration to allow sufficient time for the temperature profile of the existing joint to approach the temperature of the heated element. Following the pause, the extrusion of the subsequent segment commences. These strategic heat exchanges are expressed as geometric rules that are incorporated into the programme automating the conversion of LCM geometry into the robotic printing instructions. The expanded rule set, which also encompasses operations achieving various fabrication objectives, are illustrated and explained respectively in Tables 3 and 4. These rules include (1) *punch*, and *pull*; (2) *loop*; and (3) *offset* – procedures respectively devised to achieve filament reheating and compaction, contact area enlargement, and collision and deformation mitigation. A comparison of the joint tool-path design between the initial robotic implementation and the revised implementation with the proposed rules applied are illustrated in Table 5.

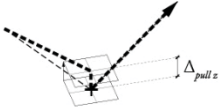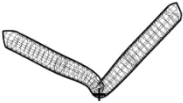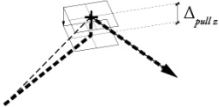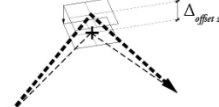**Table 3**   Geometric rules modifying imported LCM centre-lines for fabrication
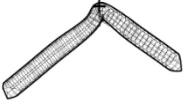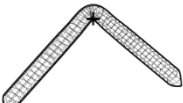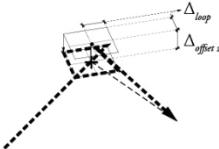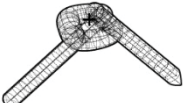
Rule	Centre-line geometry	Path modification	Filament profile
R-P1 Punch			
R-P2 Pull			
R-O Offset			
R-L Loop			

Table 4   Detailed explanation of fabrication-based geometric rules

| Rule	Descriptions
R-P1 *Punch*	Illustrated in Table 3.R-P1, punch is a mechanism pressing an incoming filament onto the existing joint. The procedure is incorporated at the end of the extrusion of downward-, or negatively sloped segments to prolong both the exposure and contact of the interfacing filament to the heated nozzle under pressure – thereby allowing the existing joint to be reheated to enable better bond formation between the interfacing layers of filament. In terminating the extrusion of the incoming filament at a position that is slightly offset in the positive vertical direction from the modelled nodal position, the procedure shortens the segment, so that the punch can stretch, straighten, and pretension the segment, which helps mitigates the length-wise deformation of the incoming segment.
R-P2 *Pull*	The geometrically mirrored operation of *punch* is *pull*, which is applied to upward-, or positively sloped segments that are approaching an existing joint from below (Table 3.R-P2). Similar to punch, the extrusion of the segment is terminated at a position that is slightly offset in the negative Z direction – thereby allowing the retraction of the extruder to pretension and straighten the incoming segment onto the existing joint.
R-O *Offset*	Offset (Table 3.R-O) is a rule designated to (1) compensate for the accumulated global vertical displacement of the nodal positions due to sagging; and to (2) minimise the collision of filaments due to the introduction of material thickness to the LCM centre-line geometry. The rule is equivalent to the basic offsetting procedure incorporated in the initial method as described in the earlier section.
R-L *Loop*	Loop, which is shown in Table 3.R-L, is a rule incorporated into the extrusion of the *supported chain* immediately placed below a *base chain* (see 'TP.$_{IK,S1}$' and 'TP.$_{JK,S1}$' in Figure 18(2)). In contrast to the other rules relying solely on the vertical displacement of the tool-path from the original centre-line model, the rule programmes an incoming nozzle to surrounding the targeted existing joint according to an offset distance determined by calibration. Next, the nozzle retracts in the positive vertical direction before it commences the extrusion of the subsequent segment. As Table 3.R-L and Table 5 (in 'Joint Detail') shows, the enlarged joint platform created by the additional material increases the contact surface area for adhesion between the platform and the subsequent chains applied onto it.

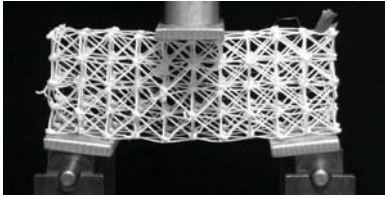## 6.4   Revised implementation

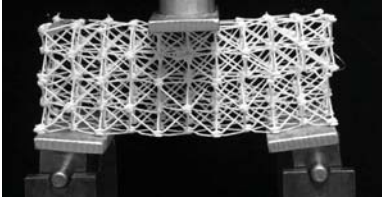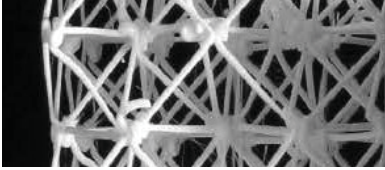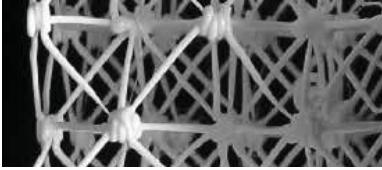### 6.4.1   Load testing and results

Based on the two implementation versions described above, a total of eight standardised regular LCM block as specified in Figure 20 were manufactured: four printed using the original implementation method (LAT-A-#), and four using the improved implementation described above (LAT-B-#). A comparative load testing, which is recorded in Figure 25, was completed in order to physically validate the structural improvement of the new implementation. The specimen were structurally tested using a single centralised vertical point load applied at the mid-span of the LCM block until a peak load was reached. Photographical documentation and performance summary of the produced specimens for each of the two implementation versions are presented in Table 6.

Table 5   Comparison of the geometric tool-path modifications applied to a typical unit-cell octet-truss module between the initial and revised method
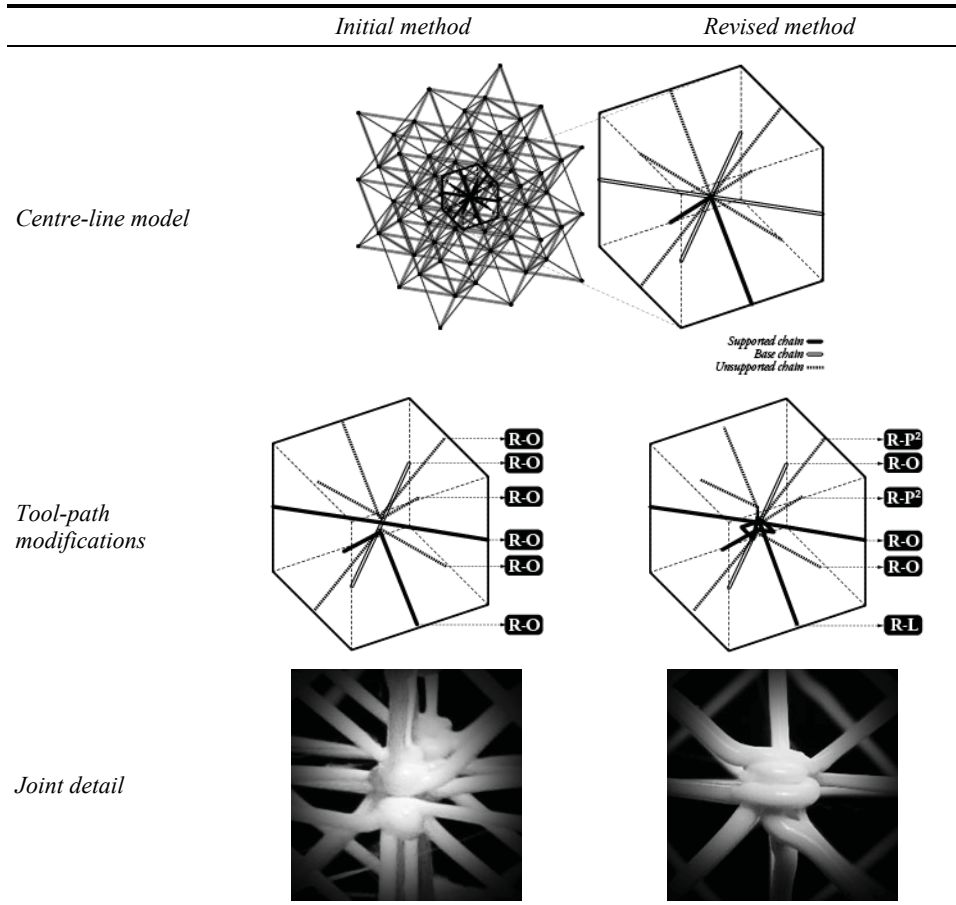
As Table 6 shows, the normalised ultimate and yield load-to-weight ratios for LAT-B specimens are respectively on average 76.6% and 69.5% higher than LAT-A's ratios. Furthermore, the stiffness of LAT-B – as indicated by the slopes of the specimens' load-displacement curves at Figure 26(2) and their median stiffness in the box-plot of Figure 26(3) – is greater than LAT-A by 71.5%. The significant performance difference indicates that the revised implementation, which focused on improving the bonding quality of the joints, has achieved some success at increasing the structural strength and stiffness of specimens produced using the proposed AM technique. Support for this interpretation is also evident when comparing the specimens' failure mode: Figure 26(2) shows that LAT-A specimens experienced multiple, periodic and simultaneous localised failures due to joint delaminations in their initial stage of load applications even when the specimens were still undergoing linear elastic deformation. In contrast, the failures of LAT-B specimens were largely due to buckling of members occurring when the specimens were approaching their yield capacity – thereby confirming that the LCM produced with the revised method is able to produce robust joint conditions that utilise the material strength of the filament with greater effectiveness and consistency.

Table 6 Documentation of the fabrication and load testing results

Name	Initial method				Revised method			
	L-A-1	*L-A-2*	*L-A-3*	*L-A-4*	*L-B-1*	*L-B-2*	*L-B-3*	*L-B-4*
Fabricated result								
Detailed close-up								
Mass (N)	0.216	0.216	0.225	0.225	0.225	0.225	0.225	0.206
Normalised yield strength-to-weight ratio	355.5	183.6	115.9	253.6	499.1	378.6	423.5	578.0
Average (N/N)	*227.2*				*469.8*			
Normalised peak strength-to-weight ratio	402.1	275.4	234.2	256.3	547.7	495.2	423.5	596.5
Average (N/N)	*292.0*				*515.5*			
Peak/Yield	1.29				1.10			
Stiffness	183.8	167.1	116.4	123.3	289.5	257.8	261.1	205.2
Average ([N/N]/mm)	*147.7*				*253.4*			
Failure mode	Buckling, with some joint failures				Buckling, with some joint failures			

6.4.2 *Calibration of computational model using Euler's buckling equation*

While the efficacy of the revised fabrication method in producing LCM with improved strength and stiffness is established, the developed specimens still underperformed by approximately 30% in comparison to the FEA results. The discrepancy suggest a need to calibrate the inputs used to construct the FEA model, so that reliable optimisation and analytical results can be obtained. This subsection uses Euler's buckling equation to infer and quantify the structural behaviour of the joints.

In structural engineering, buckling is a structural instability characterised by a sudden sideways failure of a structural member subjected to high compressive stress (Timoshenko and Gere, 1963), where the compressive stress at the point of failure is less than the ultimate compressive stress that the material is capable of withstanding. Equation (3) presents the formula Leonhard Euler derived that gives the maximum axial

load a member can carry without buckling. It can be seen that Euler's formulation is highly sensitive to k – varying by a multiple of 16. The factor accounts for the rigidity of a member's end conditions, which depends on its fabrication quality. Using buckling analysis, it is therefore possible to infer, quantify, and compare the mechanical strength of the LCM attributed to the performance its joints.

$$F = \frac{\pi^2 EI}{(KL)^2}$$
(3)

F = maximum or critical force (vertical load on column)

E = Young's modulus

I = area moment of inertia of the cross section of the rod

L = unsupported length of column

k = column effective length factor.

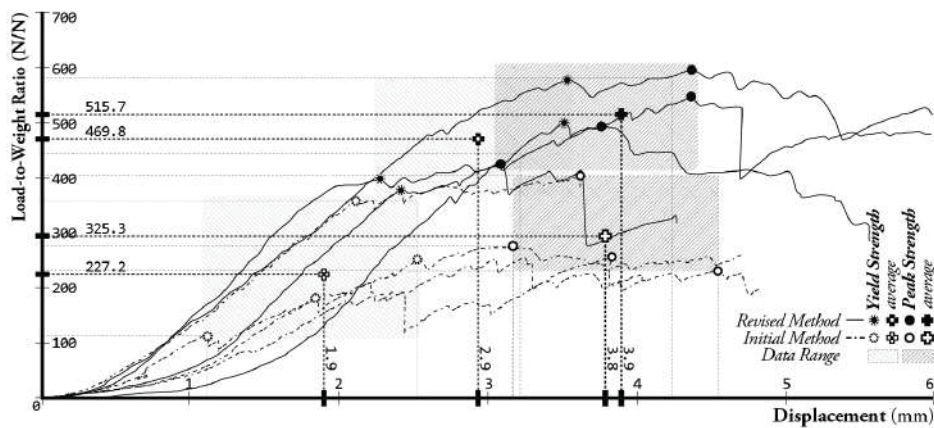**Figure 25** Load-displacement plot of all test cases

Figure 26 Comparison of load testing results between specimens produced using the initial and revised fabrication method: (1) box plot showing normalised load-to-weight yield and peak strength; and (2) load-displacement plot showing the linear-elastic portion of the load tests to provide an estimate on the specimens' elastic stiffness, which are also summarised using a (3) box plot
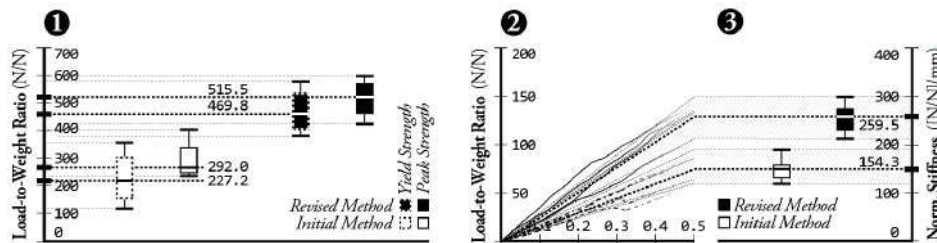

Figure 27 compares the initial yield load testing results of the LCM specimens produced using the initial and revised method (Figure 27(1)) with the FEA-predicted initial yield

loads for the equivalent LCM for a variety of *k* values (Figure 27(2)) – showing that the improvement to joint rigidity in specimens produced by the new method is equivalent to decrease of 0.30 in *k*, which is analogous to change from partially fixed hinge to partially rotatable fixed connections. The results quantify the capacity of the parts produced by the revised fabrication method to act with greater effectiveness in bending – parts that can be modelled with a revised *k* factor of 0.65 in the FEA model.

Figure 27 Comparison of experimental and FEA results: (1) actual normalised yield strength results from structural load testing, and (2) yield strength predicted with FEA using various buckling *k*-factors, which are related to (3) member end conditions consisting of (a) fixed and (b) hinged connections
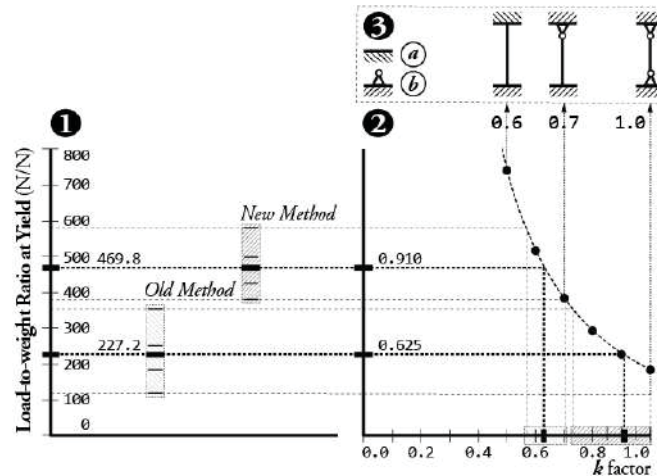

7 Design case study

A final design case study was conducted to develop an integrated design-fabrication workflow incorporating the revised robotic fabrication method and the computational generation and optimisation techniques proposed. Figure 28(1.a) illustrates the domain specification of the design case study with key geometrical descriptors. To provide a complex and realistic structural configuration for understanding the effects of topology, the final test case was specified as a double overhanging simply supported lattice-beam with load applied uniformly across all nodes at the top surface.

7.1 Characterisation of design case and optimisation strategy

Empirically determined robotic considerations informed the case study design initialisation and characterisation, which include – as explained in Section 4.3.1– the dimension of the structure and the targeted average unit-cell density. Setting the design problem bisymmetrical about the global XZ and YZ planes, at its centroid the 228-node, 2976-element, and $18 \times 3 \times 2$ LCM design space can be simplified to varying only one quarter of the beam-lattice's volume. Figure 28 identifies the 22 design variables used to characterise the LCM beam, which can be categorised as parameters that modified the LCM global geometry, and variables for creating the parameter space governing the

LCM's density. As Figure 28(1) shows, the 12 global geometry variables assigns movement along either the Y- or Z- global world axis (Figure 28(1.c)) for nine control points used to construct the LCM's design volume. Figure 28(2) shows the 10 remaining variables being used to define the 10 control points that generated the 3 NURBS-based functions governing the spacing for each row of unit-cells along the *I*-, *J*-, and *K*- axis of the LCM case study design (Figure 28 (1.b)). All variables are expressed as real number within the domain of (–1,00,1.00), which are then multiplied by a pre-defined constant referring to the maximum allowable translation distance of 0.10m for the geometrical parameters, and the maximum relative spacing multiple of 5 for the density-controlling variables.

Figure 28 Diagram outlining the LCM beam's characterisation by design variables, which include controls for (1) NURBS-based parameterisation of global geometry and (2) internal unit-cell spacing variation. Illustrated in (2.B) is a scaled representation of the optimised density distribution for each of the LCM's three primary axes according to the manipulation of the (2.A) NURBS-based functions defining the LCM's subdivision spacing increments
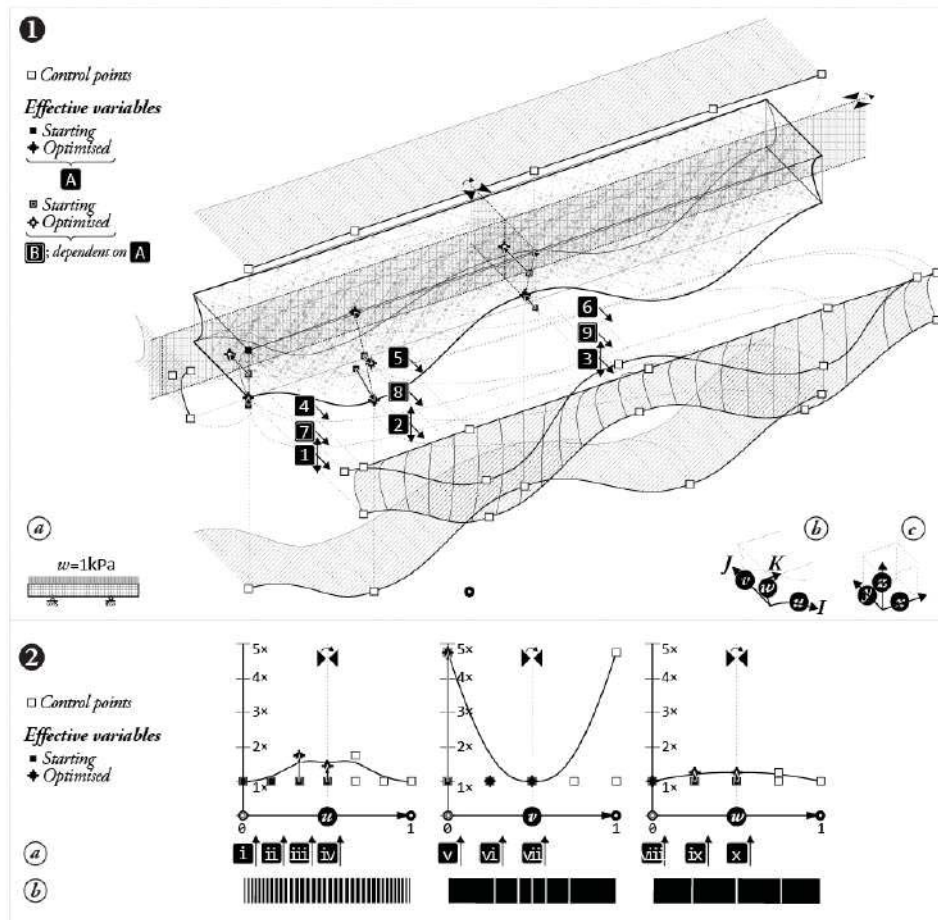
NURBS-based curves are created from the 9 control points defined by the 12 design variables – curves that are transformed, duplicated and arranged in the design model space to create the network of curvatures constructing the six NURBS surfaces defining the tetrahedral-like closed LCM beam volume. The construction of the design volume is followed by the interpolation of the 3-D grid points using the procedure described at Section 3.3.2. To reduce load concentration at the support, the 3-D grid is post-processed to ensure flat platform are generated for each of the support covering at least $1 \times 3 \times 1$ rows of unit-cells. To further improve the tractability of the 22-variable design problem, the design variables were grouped for three optimisation stages each focusing on specific structural design aspect of the LCM beam, such as its (1) structural depth (Figure 28(1.1-3): Z-axis translation); (2) width (Figure 28(1.4-9): Y-axis translation); and (3) subdivision spacing (Figure 28(2.i-x)). A brief optimisation using genetic algorithm (GA) was applied initially to provide a diverse sampling of the design space. Identifying high-performance candidates, the three classes of optimisation are then applied in the order identified above – beginning similarly with a brief application of GA, followed by an extensive gradient-based optimisation to identify the local optimum variable settings. The final morphed LCM beam has recorded a 43% gain in its stiffness-to-weight ratio – as measured by the normalised strain energy Figure 30 shows.

Figure 29 Orthographic documentation of the LCM beam structurally optimised using the proposed global morphing techniques (GMT): (1) cross section view; (2) plan view and (3) elevation view
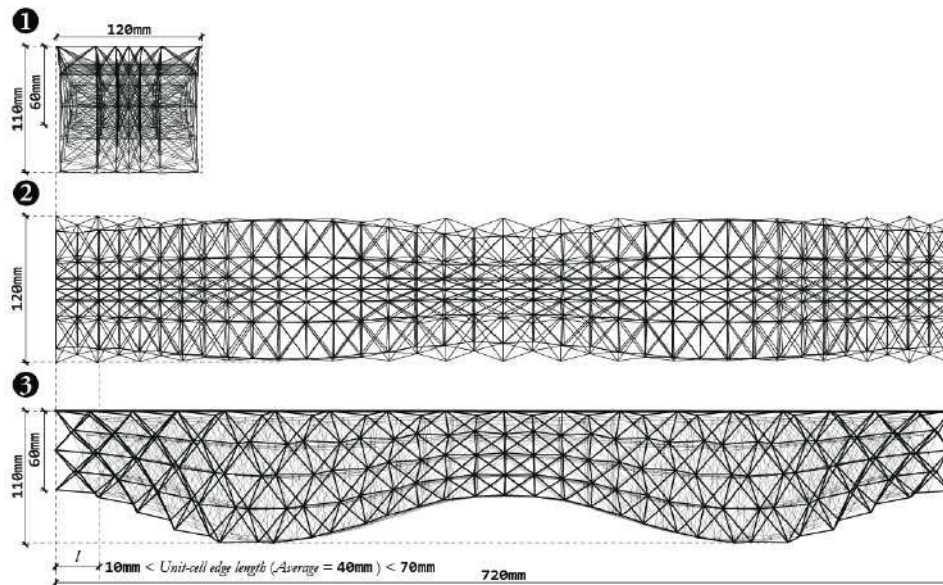
7.2 Fabrication and results

Following the revised fabrication methodology outlined in Implementation III, the final LCM beam was decomposed into 4 individual print programmes – each corresponding to a half-layer of unit-cells within the 2-layer LCM beam. To minimise cantilevering of the global geometry during the extrusion process, the LCM beam was printed upside down with its top surface aligned on the printing bed, as shown in Figure 31. A duration of 12 hours was required to extrude the LCM beam measuring 86.79 m in total filament length.

The images in Figure 32 demonstrates that the revised fabrication method is relatively successful at materialising the morphed LCM with good geometrical fidelity. There is a small degree of imperfection and variability (Figure 33(top)), such as residual filament release, occasional member sagging and excessive extrusion at the joints, which could be reduced as the process is further improved. The structure is stiff to the touch and there appears to be sufficient bonding between the interfacing member segments at the joints.

Figure 30 Image sequence showing increasing gains in stiffness as the input LCM block is morphed into the final optimised geometry
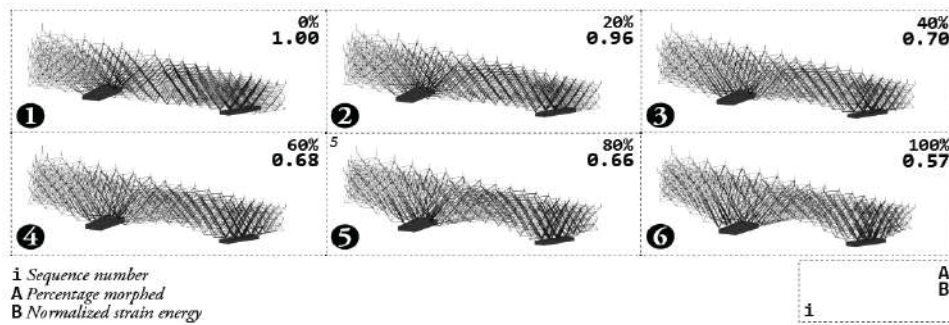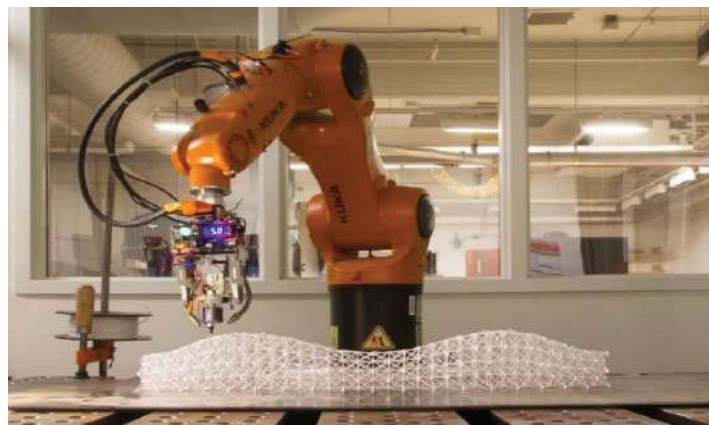

Figure 31 Photograph showing the robotic fabrication of the design case (see online version for colours)

7.3 Structural load testing and discussion

A structural load testing was completed on the printed LCM beam to validate the performance of the design case, as demonstrated in Figure 33. To evenly distribute the loads across all nodes at the beam's top surface, the load is applied mid-span through an aluminium plate placed on top of a bar spanning across the top surface of the LCM beam. Similarly, the two flat support faces of the LCM beam are seated on two metal platforms. The beam-lattice was tested until the second yield point, which corresponds to the failure of a second member in the system.

Figure 32 Photographic documentation of case study: (top) detail of joints; (middle) elevation view; and (bottom) plan view
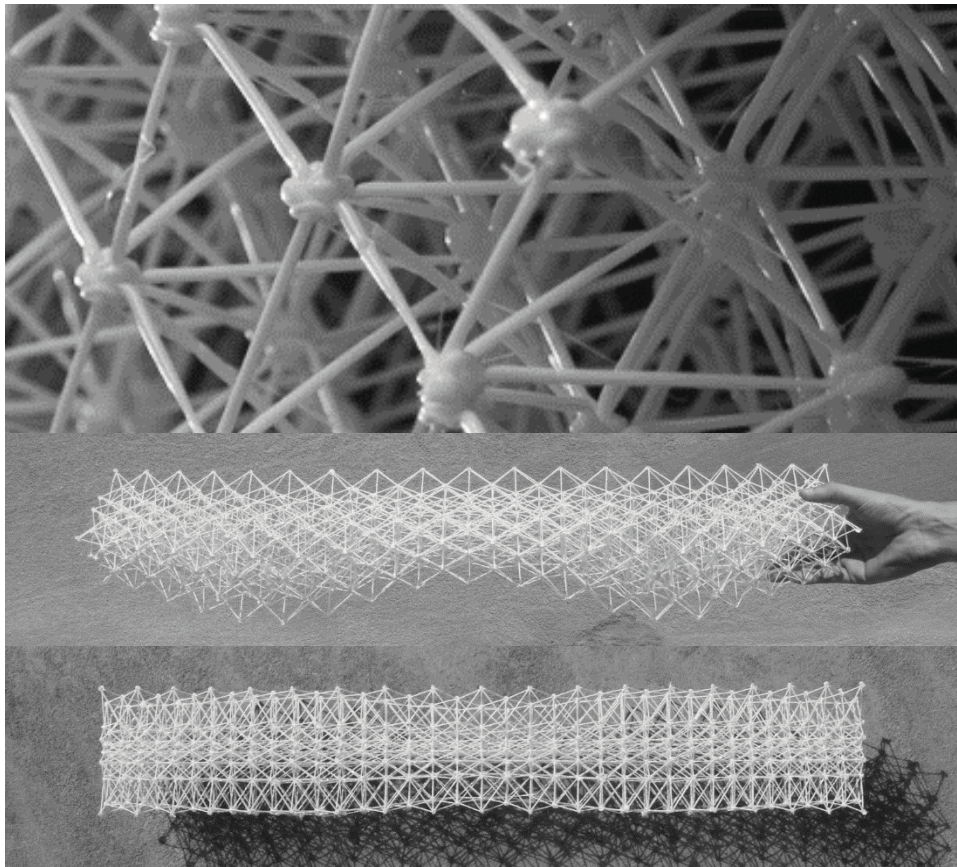
With an initial strength-to-weight yield capacity of 113.6 (N/N), as indicated in the load-displacement plot illustrated by Figure 34, the actual strength capacity of the lattice-load beam is within 12.6% of the LCM beam's FEA-determined capacity of 129.44 (N/N). The closeness in the numerical and experimental results demonstrate the effectiveness of the revised fabrication method in achieving structurally and mechanically consistent results, and confirms the accuracy of the preceding section's proposed calibration

method. There is however large discrepancy in expected stiffness, as the maximum displacement of the printed specimen, which measures 3.31mm, is effectively 117.8% the numerically predicted amount of 1.52mm. A number of factors may account for this difference, including (1) inaccuracy in the material property used to estimate the commercially purchased PLA material, (2) remaining imperfection of the fabrication process, and (3) unaccounted non-linear behaviour due to large deformation.

Figure 33 Photograph showing the load-testing setup and execution (see online version for colours)
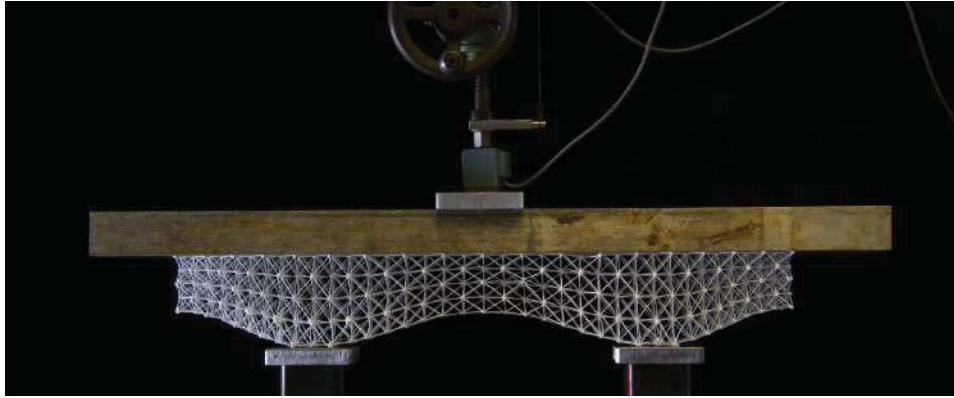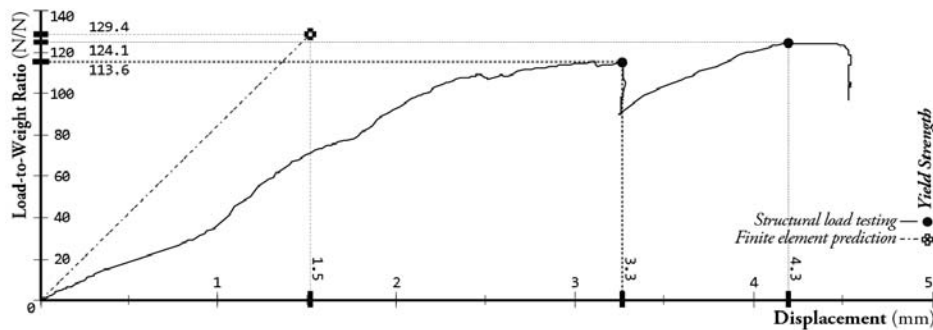

Figure 34 Load-displacement plot for the LCM beam design case – showing both load testing and FEA-prediction results

Despite of the discrepancies, the investigations nevertheless provides evidence that the proposed LCM design, optimisation and fabrication framework is relatively successful at achieving geometrically complex LCM that is morphed according to structural efficiency. However, the encouraging results seen in the object-scale implementation will not be directly transferable to the fabrication of full-scale structures. The comparison of results between the test specimens of Implementation III and the design case shows a substantial reduction in the latter cases' initial yield load-to-weight capacity by a factor of 4. The performance difference exposes the scalability limitation of the current fabrication method, which can only produce members at a single cross section. Thus, the increase in the LCM's design volume translates to a decrease in the load-to-weight capacity, as the maximum allowable member force remains unchanged regardless of geometrical scale

and load magnitudes. A retrospective investigation by the authors have quantified the unrealised structural efficiency due to the cross section restriction: results from preliminary sizing optimisation show that – using three discrete cross sections – the same load capacity may be achieved with a 54% reduction in material, whereas a 73% increase in load capacity is achievable with the same total quantity of print material. Thus, future improvements to the fabrication technique, such as the use of material with superior strength and stiffness properties and the upgrading of hardware to support cross section variability, will help realise the theoretical benefits of applying lattice-based design discretisation and structurally informed morphing.

8 Conclusion

The research pursued in this paper develops, documents, and validates a consolidated and holistic design-fabrication framework combining the benefits of robotics-enabled AM with lattice-based discretisation that creates light-weight and high-performance additive manufacturable parts composed of LCM. The integration of the two concepts provided a strategy to tackle two known mechanical limitations confronting additive manufacturing. In extruding the thermoplastic filament in 3-D space along paths, or lattice members optimised to encompass a structural system's preferred and efficient load paths, the proposed technique (1) ensures the alignment of structural members and filament orientation, which eliminates the problem of anisotropy, and (2) integrates the design of a printed part with its decomposition as printing paths or instructions – thereby unifying the consideration of structural behaviour at the various design scales of the printed part. Specifically, the research proposed new computational techniques to address the current lack of methods for considering the fabrication process in optimisation, and for complex geometries with large number of design elements and variables. In contrast to similar work, an iterative process of physical fabrication implementation and empirical load testing were heavily incorporated into the research methodology to identify opportunities for calibrating both computational and fabrication parameters, in order to improve the accuracy of the generative and analytical models, and to increase the strength and stiffness of the produced parts. Finally, a design case was presented to provide a full demonstration on how the proposed design-fabrication workflow developed in this paper can seamlessly enable designers to conceive and materialise LCM parts – validating the simplicity and efficacy of the design characterisation and optimisation methods, and confirming the reliability of the fabrication process in producing quality and high-performance LCM parts with complexly morphed geometries. This performance supports the potential of 3D printing as a means of fabrication that combines structurally driven geometry with complexity-agnostic materialisation in new and exciting ways.

Acknowledgement

References

Abd El Malek, M., Senousy, M., Hegazi, H. and Metwalli, S. (2005) 'Heuristic gradient projection for 3D space frame optimization', *ASME International Design Engineering Technical Conferences and Computers in Engineering Conference, (Design Automation Conference)*, Boston, MA, pp.337–344.

Achtziger, W. (1997) 'Topology optimization of discrete structures: an introduction in view of computational', *Topology Optimization in Structural Mechanics*, Springer, Vienna, Austria, pp.57–100.

Allaire, G. (2002) *Shape Optimization by the Homogenization Method*, Springer-Verlag New York, New York City, NY.

Ashby, M. (2000) *Metals Foams: A Design Guide*, Butterworth-Heinemann, Woburn, MA.

Ashby, M. and Gibson, L. (1983) 'The mechanical properties of cellular solids', *Metallurgical Transactions A*, Vol. 14A, pp.1755–1769.

Bendsøe, M. (1995) *Optimization of Structural Topology, Shape and Material*, Springer Berlin Heidelberg, Berlin, DEU.

Bendsøe, M. and Kikuchi, N. (1988) 'Generating optimal topologies in structural design using a homogenization', *Computer Methods in Applied Mechanics and Engineering*, Vol. 71, pp.197–224.

Bendsøe, M. and Sigmund, O. (2002) *Topology Optimization: Theory, Methods and Applications*, Springer, Berlin, DEU.

Bennett, J. and Botkin, M. (1985) 'Structural shape optimization with geometric description and adaptive mesh refinement', *Aerospace Research Central*, Vol. 23, No. 3, pp.458–464.

Beyer, C. and Figueroa, D. (2016) 'Design and analysis of lattice structures for additive manufacturing', *Journal of Manufacturing Science and Engineering*, Vol. 138, No. 12.

Brackett, D., Ashcroft, I. and Hague, R. (2011) 'Topology optimization for additive manufacturing', *Solid Freeform Fabrication (SFF) Symposium*, Austin, Texas, USA.

Branch Technology (2017) *Branch Technology* [Online], Available at: http://www.branch.technology/ (Accessed 30 04 2017).

Braumann, J. and Brell-Cokcan, S. (2011) Parametric robot control: INTEGRATED CAD/CAM For ARCHITECTURAL DESIGN', *Proceedings of the 31st Annual Conference of the Association for Computer Aided Design in Architecture*, Calgary, AB, pp.242–251.

Cervera, E. and Trevelyan, J. (2005) 'Evolutionary structural optimisation based on boundary representation of NURBS. Part II: 3D algorithms', *Computers and Structures*, Vol. 83, pp.1917–1929.

Chang, K. and Tang, P. (2001) 'Integration of design and manufacturing for structural shape opitimization', *Advances in Engineering Software*, Vol. 32, No. 7, pp.555–567.

Chang, P. (2010) *An Improved Size, Matching, and Scaling Synthesis Method for the Design of Meso-Scale*, Unpublished Master's thesis, Georgia Institute of Technology, Atlanta, Georgia, United States of America.

Cheung, K. and Gershenfeld, N. (2013) 'Reversibly assembled cellular composite materials', *Science*, Vol. 341, pp.1229–1221.

Chilton, J. (2000) *Space Grid Structures*, Architectural Press, Oxford, Great Britain.

Clune, R., Kelliher, D., Robinson, J. and Campbell, J. (2014) 'NURBS modeling and structural shape optimization of cardiovascular stents', *Structural and Multidisciplinary Optimization*, Vol. 50, No. 1, pp.159–168.

Danhaive, R. and Mueller, C. (2015) 'Combining parametric modeling and interactive optimization for high-performance and creative structural design', *Proceedings of the International Association for Shell and Spatial Structures (IASS) Symposium 2015*, Amsterdam, NLD.

Deshpande, V., Fleck, N. and Ashby, M. (2001) 'Effective properties of the octet-truss lattice material', *Journal of the Mechanics and Physics of Solids*, Vol. 49, pp.1747–1769.

Desphande, V., Ashby, M. and Fleck, N. (2001) 'Foam topology bending versus stretching dominated architectures', *Acta Mater.*, Vol. 49, pp.1035–1040.

Doubrovski, Z., Verlinden, J. and Geraedts, J. (2011) 'Optimal design for additive manufacturing: opportunities and challenges', *ASME 2011 International Design Engineering Technical Conferences & Computers and Information in Engineering Conference IDETC/CIE 2011*, Washington, DC, USA, pp.635–646.

Evans, A.G., Hutchinson, J.W., Fleck, N.A., Ashby, M.F. and Wadley, H.N.G. (2001) 'The topological design of multifunctional cellular metals', *Progress in Materials Science*, Vol. 46, pp.309–327.

Festo (2017) *3D Cocooner | Festo Corporate* [Online], Available at: https://www.festo.com/group/en/cms/11958.htm (Accessed 21 04 2017).

Fuller, R. (1961) *Synergetic Building Construction*, United States of America, Patent No. 2, 986, 241.

Gibson, I., Rosen, D. and Stucker, B. (2010) *Additive Manufacturing Technologies: Rapid Prototyping to Direct Digital Manufacturing*, Springer Science & Business Media, New York City, NY.

Gibson, L.J. and Ashby, M.F. (1999) *Cellular Solids: Structure and Properties*, 2nd ed., Cambridge University Press, Cambridge.

Hack, N. and Laurer, W. (2014) 'Mesh-mould: robotically fabricated spatial meshes as reinforced concrete formwork', *Architectural Design*, Vol. 84, No. 3, pp.44–53.

Hague, R., Campbell, I. and Dickens, P. (2003) 'Implications on design of rapid manufacturing', *Proceedings of the Institution of Mechanical Engineers, Part C: Journal of Mechanical Engineering Science*, Vol. 217, No. 1, pp.25–30.

ICD, I.f.C.D.a.C. (2015) *ICD/ITKE Research Pavilion 2014-15* [Online], Available at: http://icd.uni-stuttgart.de/?p=12965 (Accessed 30 04 2017).

Jenett, B. (2015) *Digital Material Aerospace Structures*, Massachusetts Institute of Technology, Cambridge, Massachusetts, USA.

Jenett, B., Cellucci, D., Gregg, C. and Cheung, K. (2016) 'Meso-scale digital materials: modular, reconfigurable, lattice-based structures', *ASME 2016 11th International Manufacturing Science and Engineering Conference. Volume 2: Materials; Biomanufacturing; Properties, Applications and Systems; Sustainable Manufacturing*, Blacksburg, VA.

Jin, Y., He, Y. and Fu, J. (2013) 'An adaptive tool path generation for fused deposition modeling', *Advanced Material Research*, Vol. 819, pp.7–12.

Johnson, S. (2017) *NLopt – AbInitio* [Online], Available at: http://ab-initio.mit.edu/wiki/index.php/NLopt (Accessed 30 04 2017).

Johnston, S., Reed, M., Wang, H. and Rosen, D. (2006) *Analysis of Mesostructure Unit Cells Comprised of Octet-Truss Structures*, Georgia Institute of Technology, s.l.

Leary, M., Merli, L., Torti, F., Mazur, M. and Brandt, M. (2014) 'Optimal topology for additive manufacture: a method for enabling additive manufacture of support-free optimal structures', *Materials and Design*, Vol. 63, pp.678–690.

Leary, M., Babaee, M., Brandt, M. and Subic, A. (2013) 'Feasible build orientations for self-supporting fuse-deposition manufacture: a novel approach to spacefilling tessellated geometrics', *Advanced Materials Research*, Vol. 633, pp.144–168.

Li, Y., Chen, Y. and Zhou, C. (2009) 'Design of flexible skin for target displacements based on meso-structures', *Proceedings of the American Society of Mechanical Engineers (ASME) 2010 International Design Engineering Technical Conferences & Computers and Information in Engineering Conference*, San Diego, CA, pp.611–624.

Lu, K. and Kota, S. (2006) 'Topology and dimensional synthesis of compliant mechanism using discrete', *ASME Journal of Mechanical Design*, Vol. 128, pp.1080–1091.

MatterHackers (2013) *How to Succeed When Printing in PLA | MatterHackers* [Online], Available at: http://www.matterhackers.com/articles/how-to-succeed-when-printing-in-pla (Accessed 30 04 2017).

Michalatos, P. and Kaijima, S. (2014) 'Eigenshells', in Adriaenssens, S., Block, P., Veenendaal, D. and Williams, C. (Eds.): *Shell Structures for Architecture: Form Finding and Optimization*, Routledge, Abingdon, ENG, pp.195–210.

Mueller, C.T. and Ochsendorf, J. (2015) 'Combining structural performance and designer preferences in evolutionary design space exploration', *Automation in Construction*, Vol. 52, pp.70–82.

Narkis, M. (1979) 'Sintering behavior of poly(methylmethacrylate) particles', *Polymer Engineering & Science*, Vol. 19, No. 13, pp.889–992.

Nguyen, J., Park, S-I., Rosen, D.W., Folgar, L. and Williams, J. (2012) 'Conformal lattice structure design and fabrication', *Solid Freeform Fabrication Symposium*, Austin, TX, pp.138–161.

Pedersen, P. (2000) 'On optimal shapes in materials and structures', *Structure Mutlidisciplinary Optimization*, Vol. 19, pp.169–182.

Preisinger, C. (2017) *karamba 3d* [Online], Available at: http://www.karamba3d.com/ (Accessed 30 04 2017).

Rafael, A. (2010) *Poly(Lactic Acid): Synthesis, Structures, Properties, Processing, and Applications*, Wiley, Hoboken, NJ.

Reas, C., Fry, B. and Maeda, J. (2007) *Processing: A Programming Handbook for Visual Designers and Artists*, 2015 ed., MIT Press, Cambridge, MA.

Rechenraum (2017) *rechenraum – Download* [Online], Available at: http://www.rechenraum.com/goat/download.html (Accessed 30 04 2017).

Robert McNeel & Associates (2017) *Rhinoceros* [Online], Available at: https://www.rhino3d.com/ (Accessed 30 04 2017).

Rosen, D.W. (2007) 'Computer-aided design for additive manufacturing of cellular structures', *Computer-Aided Design & Applications*, Vol. 4, No. 5, pp.585–594.

Rozvany, G.I.N., Bendsøe, M.P. and Kirsch, U. (1995) 'Layout optimization of structures', *Applied Mechanics Reviews*, Vol. 48, No. 2, pp.41–119.

Schumacher, C., Bickel, B., Rys, J., Marschner, S., Daraio, C. and Gross, M. (2015) 'Microstructures to control elasticity in 3D printing', *ACM Transactions on Graphics (TOG)*, Vol. 34, No. 4, p.136.

Shepherd, P. and Richens, P. (2009) 'Subdivision surface modeling for architecture', *Proceedings of the International Association for Shell and Spatial Structures (IASS) Symposium 2009*, Valencia, ESP.

Shiffman, D. (2015) *Learning Processing : A Beginner's Guide to Programming Images, Animation, and Interaction*, Morgan Kaufmann, Amsterdam, NLD.

Shiffman, D., Fry, S. and Marsh, Z. (2012) *The Nature of Code*, D. Shiffman, New York City, NY.

Sun, Q., Rizvi, G., Bellehumeur, C. and Gu, P. (2008) 'Effect of processing conditions on the bonding quality of FDM polymer filaments', *Rapid Prototyping Journal*, Vol. 14, No. 2, pp.72–80.

Svanberg, K. (1994) 'Global convergence of the stress ratio method for truss sizing', *Structural and Multidisciplinary Optimization*, Vol. 8, pp.60–68.

Takezawa, A., Nishiwaki, S.K.I. and Yoshimura, M. (2005) 'Structural topology opitmization using frame elements based on the complemntary strain energy concept for eigen-frequency maximization', *Proceedings of the American Society of Mechanical Engineer (ASME) 2005 International Design Engineering Technical Conferences & Computers and Information in Engineering Conference*, Long Beach, CA, pp.909–919.

Tam, K-M.M. and Mueller, C. (2017) '3D printing and additive manufacturing. Additive manufacturing along principal stress lines: structurally informed material deposition and toolpath planning', *3D Printing and Additive Manufacturing*, Vol. 4, No. 2, pp.63–81.

Tam, K-M.M., Coleman, J.R., Mueller, C.T. and Fine, N. (2016) 'Stress line additive manufacturing (SLAM) for 2.5-D shells', *Journal of the International Association for Shell and Spatial Structures*, Vol. 57, No. 4, pp.249–259.

Tam, K-M.M., Coleman, J.R., Mueller, C.T. and Fine, N. (2017a) 'Robotics-enabled stress line additive manufacturing', in Dagmar, R., Saunders, R. and Burry, J. (Eds.): *Proceedings of the 3rd Robotic Fabrication in Architecture, Art and Design (Rob|Arch) Conference*, Springer, Cham, Switzerland, pp.351–362.

Tam, K-M.M., Reynolds, D.V., Poulsen, E. and Otani, R. (2017b) 'Equivalent material modelling of complex additive manufactured conformal lattices', *Proceedings of the International Association of Shell and Spatial Structures (IASS) Symposium 2017*, Hamburg.

Timoshenko, S. and Gere, J. (1963) *Theory of Elastic Stability*, McGraw-Hill Book Company, New York City, NY.

Topping, B. (1993) 'Topology design of discrete structures', *Topology Design of Structures*, Kluwer Academic Publishers, Dordrecht, NLD, pp.517–534.

Wall, W., Frenzel, M. and Cyron, C. (2008) 'Isogeometric structural shape optimization', *Computer Methods in Applied Mechanics and Engineering*, Vol. 197, Nos. 33–40, pp.2976–2988.

Weeger, O., Kang, Y. and Yeung, S-K.D.M. (2016) 'Optimal design and manufacture of active rod structures with spatially variable materials', *3D Printing and Additive Manufacturing*, Vol. 3, No. 4, pp.204–215.

Williams, C.B., Mistree, F. and Rosen, D.W. (2005) 'Investigation of solid freeform fabrication processes for the manufacture of parts with designed mesostructure', *DETC05: ASME 2005 Design Engineering Technical Conferences and Computer and Information in Engineering Conference*, Long Beach, California, pp.586–596.

Willmann, J., Gramazio, F., Kohler, M. and Langenberg, S. (n.d.) *Digital by Material. Envisioning an Extended Performative Materiality in the Digital Age of Architecture*, ETH Zurich, s.l.

Zhou, H. (2010) 'Topology optimization of compliant mechanism using hybrid discretization model', *Proceedings of the American Society of Mechanical Engineers (ASME) 2010 International Design Engineering Technical Conferences & Computers and Information in Engineering Conference*, Montréal, QC.

Bibliography

Chen, Y., Kwok, T-H. and Li, Y. (2016) 'A structural topology design method based on principal stress line', *Computer-Aided Design*, Vol. 80, pp.19–31.

Graf, G.C., Chu, J., Engelbrecht, S. and Rosen, D.W. (2009) 'Synthesis methods for lightweight lattice structures', *ASME 2009 International Design Engineering Technical Conferences Computers and Information in Engineering Conference IDETC/CIE 2009*, San Diego, Califronia, USA, pp.579–589.

Kane, J., Zhao, G., Wang, H. and Guru Prasad, K. (1992) 'Boundary formulations for three-dimensional continuum structural shape sensitivity analysis', *Journal of Applied Mechanics*, Vol. 59, pp.827–834.

KUKA AG (2017) *KR AGILUS sixx | KUKA AG* [Online], Available at: https://www.kuka.com/en-us/products/robotics-systems/industrial-robots/kr-agilus-sixx (Accessed 30 04 2017).

Rodríguez, J.F., Thomas, J.P. and Renaud, J.E. (2016) 'Mechanical behavior of acrylonitrile butadiene styrene (ABS) fused deposition materials. Experimental investigation', *Rapid Prototyping Journal*, Vol. 7, No. 3, pp.148–158.

Rosen, D., Johnston, S., Reed, M. and Wang, H. (2006) 'Design of general lattice structures for lightweight and compliance applications', *Rapid Manufacturing Conference*, Loughborough University.

Zhu, Y., Tian, X. and Li, J. (2015) 'The anisotropy of laser melting deposition additive manufacturing Ti–6.5Al–3.5Mo–1.5Zr–0.3Si titanium alloy', *Materials and Design*, Vol. 67, pp.538–542.

Ziemian, C., Sharma, M. and Ziemian, S. (2012) 'Anisotropic mechanical properties of ABS parts fabricated by fused deposition modelling', in Gokcek, M. (Ed.): *Mechanical Engineering*, InTech, pp.159–180, DOI: 10.5772/34233. Available from: https://www.intechopen.com/books/mechanical-engineering/anisotropic-mechanical-properties-of-abs-parts-fabricated-by-fused-deposition-modeling-